

NASA TT F-11,890

INVESTIGATIONS OF CRATERS BY MICROPROJECTILES AT A
VELOCITY RANGE OF 0.5 to 10 km/SECOND

Volker Rudolph

Translation of "Untersuchungen an Kratern von Mikroprojekten
im Geschwindigkeitsbereich von 0,5 bis 10 km/sec."
Dissertation, Ruprecht-Karl-University,
Heidelberg, 1967, 46 pages

FACILITY FORM 602

N 68-35737	
(ACCESSION NUMBER)	(THRU)
50	
(PAGES)	(CODE)
(NASA CR OR TMX OR AD NUMBER)	(CATEGORY)

GPO PRICE \$ _____

CSFTI PRICE(S) \$ _____

Hard copy (HC) _____

Microfiche (MF) _____

ff 653 July 65

NATIONAL AERONAUTICS AND SPACE ADMINISTRATION
WASHINGTON, D.C. 20546 SEPTEMBER 1968



TABLE OF CONTENTS

- I. Introduction
- II. General Considerations Regarding Impact of Particles at High Velocities
 - A. Classification of Tests by Projectile Velocity
 - B. Description of Crater Formation by Physical Properties
- III. Test Methods
 - A. The Acceleration of Micro-Particles
 - B. The Mass-Velocity Filter
 - C. Absolute Calibration of Projectile Parameters
 - D. Test Procedures for Evaluation of Craters
- IV. Tests
 - A. The Testing Range
 - B. General Appearance of the Craters
 - C. Crater Diameter
 - D. Measurable Crater Depth and Crater Shape
 - E. Actual Crater Depth
 - F. Crater Volume
- V. Model for Description of Craters
 - A. Model Concept
 - B. Velocity Range above the Yield Point of the Projectile
 - C. Velocity Range below the Yield Point of the Projectile
- VI. Evaluation of Test Results on the Basis of the Model Concept
 - A. Evaluation of test Results for Equal Target Materials
 - B. Dependence on Material
- VII. Comparison of Craters of cm-Projectiles and Craters of μ -Projectiles

VIII. Summary

IX. Bibliography

INVESTIGATIONS OF CRATERS BY MICROPROJECTILES AT A
VELOCITY RANGE OF 0.5 to 10 km/SECOND

Volker Rudolph, M. A. Physics, Nussloch/Heidelberg, Germany

ABSTRACT: Tests were performed to determine the shape, diameter, and depth of craters produced in Pb, Cd, Ag, Cu, and Al target materials by impact of artificially accelerated Fe - projectiles of μ -size of velocities ranging from 0.5 to 10 km/second. Formulas are derived to approximate the relationships between projectile mass, diameter, and velocity, and diameter, depth, and volume of the craters produced. The results are compared with corresponding relationships developed in earlier research for cm-size projectiles to derive similarity equations in first approximation.

1. Introduction

Cosmic dust is of great importance in the universe, as for instance in interstellar absorption, polarization, and in color changes of stellar light. /1*
Dust clouds may even be observed by the naked eye in the apparent separation of the Milky Way and in the zodiacal light of the sun.

The rapid advancement of space research makes possible closer study of cosmic dust in our solar system. At the Max-Planck-Institute of Nuclear Physics of Heidelberg, this research is carried out with the use of rockets and satellites. The research program comprises, on the one hand, the collection of cosmic dust followed by chemical analysis in the laboratory [1-5], and on the other, the development of detectors for in-flight measurement of the physical parameters of cosmic particles such as mass and velocity, and for transmission to the ground [6].

Artificially accelerated dust is used to calibrate these detectors, and to study problems encountered in connection with the collection of cosmic dust. The Van-de-Graff pressure-boiler accelerator available for artificial acceleration is different from a nuclear accelerator in that it is equipped with special apparatus, such as dust source, dust detector, and mass-velocity filter. This facility is further suited for the simulation of processes involving cosmic dust.

Particles having velocities in excess of about 0.5 km/sec form craters on impact with collecting surfaces. Because of the velocity of rockets and satellites, the relative velocity of the dust particles is generally above 0.5 km/sec. Therefore craters are to be expected when cosmic dust is being collected. Conversely, the craters are therefore also a fairly reliable means of identifying cosmic particles. As has been shown by means of artificially accelerated dust, the chemical composition of the particles can be determined by microanalysis of the craters. Further, the impact conditions of the projectiles can be deter-

*Numbers in the margin indicate pagination in the foreign text.

mined from the shape of the craters. The purpose of the subject study is to clarify these relationships, specifically by bombarding different targets with particles of a few tenths to several μ diameter at velocities of 0.5 to 10 km/sec.

Furthermore, a contribution to the knowledge about craters in general may ^{/2} be anticipated as a result of such impact experiments. The continuous function given by Baldwin [7,8] for the depth and diameter of craters produced by shells, bombs, and by dynamite explosions, and for the depth and diameter of meteorite craters on earth and of most moon craters, suggests that both impact craters and explosion craters are similar phenomena which can be interpreted using similar model concepts.

Because of the energy requirements it is impossible to accelerate projectiles of more than a few centimeters (diameter) to cosmic velocities. The smallest projectiles used to produce craters are a few $1/10 \mu$ in diameter. A large number of tests, predominantly in the range of cm-projectiles at supersonic speeds provided information on the formation of impact craters. However, due to the absence of sufficient measurements and because of the number of possible parameters, it has not been possible so far to form an adequate theory of supersonic impact, or to understand the formation of craters in the widest sense of the word. But the comparison of experiments with cm-projectiles and μ -projectiles presented at the end of the paper appears to confirm the existence of laws of similarity for the two types of projectiles.

II. General Considerations Regarding Impact Of Particles At High Velocity

A. Classification of Experiments by Projectile Velocity.

Since the appearance of craters varies conspicuously with increasing velocity, the experiments are divided into ranges of projectile velocity, as for instance high velocity impact and supersonic impact.

High velocity denotes a projectile velocity which is smaller than the sonic velocity of the target and larger than about 0.5 km/sec. The velocity of sound in metals and rocks normally amounts to several km/sec. Supersonic velocity refers to a projectile velocity larger than the sonic velocity in the target (material).

This classification should be understood on the basis of the following considerations: below the velocity of sound in the target material the results, or rather the processes, of crater formation differ substantially depending on the state of the projectile or of the target, i.e. liquid [9], brittle, or ^{/3} elastic [10]. Above the velocity of sound in the target material, these characteristics are obscured. For instance, the fragmentation effects at small projectile velocities become very important if one of the two materials is brittle (rocks) [11-14]. With increasing projectile velocity however, fragmentation becomes so fine that the process becomes similar to the case where both materials are elastic as, for example, in the case of most metals.

Based on observations of crater formation it is advisable to divide the projectile velocities for elastic materials into three intervals of increasing velocity [15]:

1. The range A in which the projectile remains intact. In this range the projectile is only slightly altered and with increasing velocity forms a crater of increasing depth with a diameter that roughly corresponds to the diameter of the projectile. This velocity range extends to about 1 km/sec.
2. The range B, or transition range. In this range, the projectile deforms more and more with increasing velocity, to the point where the remainder of the projectile is unrecognizably mixed with the crater material.
3. The range C, or liquid impact. This velocity range is above the velocity of sound in the target materials. Here the energy of the projectile substantially exceeds the internal cohesion of the reacting material, i.e. the process of crater formation appears to approach that of the impact of liquids upon liquid.

The limits between individual velocity ranges are not clearly defined, rather the transitions are gradual.

B. Description of Crater Formation by Physical Properties

In the range of 0.5 to 10 km/sec, the following observations were made for particular projectile-target combinations: upon impact of a projectile its energy is transformed in many ways. A crater with a rim is formed in the process. The shape of the crater, for instance, depends on the thickness of the target [18], on the materials involved [19,20], on the energy of the projectile, on projectile velocity, and on the direction of impact [22-26]. Within a specific zone the target material is altered, e.g. the lattice structure is destroyed [21] and the target material is hardened [17]. Both projectile material and target material is emitted, for example, in the form of droplets and fragments which have an ejection velocity comparable to the projectile velocity [30] and an ejection angle which, for example, depends on the energy of the projectile [31]. Emission of ions and electrons was also observed [27,28,6]. Light of varying wave length and intensity is emitted at the same time [32]. /4

The various phenomena observed depend in part and in complex manner on the projectile parameters. Important projectile parameters are: velocity, direction of impact, shape, thickness, and hardness. Frequently used target parameters are: velocity [35, 36], melting point, and specific heat [9]. In part, some of the parameters may be expressed in terms of other parameters, also in terms of some that are not specifically mentioned. Which of these parameters are used to describe the phenomena observed depends on the respective model [9, 39-45]. Model computations are greatly complicated by the dependence on time of the physical parameters since the instantaneous pressure upon impact of the projectile is extremely high (roughly in the order of megabars).

III. Testing Methods

In comparison to cm-projectiles, microprojectiles have the advantage that more particles can be accelerated per unit time, that the energy transformed upon impact on the target is appreciably smaller and that destruction of the measuring apparatus is therefore hardly likely to occur. Thus, several thousand μ -particles can be accelerated per hour depending on the accelerating mechanism, in contrast to several cm-projectiles per day. Disadvantages of experiments with μ -projectiles, however, are the smallness of the resulting effects, and therefore the costly test apparatus.

A. Acceleration of μ -Particles.

A 2 MV pressure boiler Van-de-Graff generator manufactured by the High Voltage Engineering Corporation is used to accelerate the μ -particles. In the dust source the particles are first heavily positively charged at a point of about 20 μ , then electrostatically accelerated, and subsequently analyzed in a detector.

The detector is in principle a cylinder condenser with an amplifier. An impulse is induced as a projectile passes through the condenser. The amplitude of the impulse is proportional to the charge q of the particle, and the impulse duration is proportional to the flight time of the projectile and therefore inversely proportional to the particle velocity v . Since /5

$$m v^2 / 2 = q U \quad (1)$$

the mass m of the projectile is uniquely defined by q and v , since the generator voltage U is known.

As the maximum charge of a particle is limited by the field intensity E_{\max} at which ion emission occurs on the surface of the projectile, the end velocity of a spherical projectile is

$$v \leq (2 U E_{\max} / (\rho_p d))^{1/2}, \quad (2)$$

where ρ_p is the projectile density and d the projectile diameter. This means that the smaller the projectile, the larger the possible end velocity. Accordingly, the charging process results in a selection according to velocity.

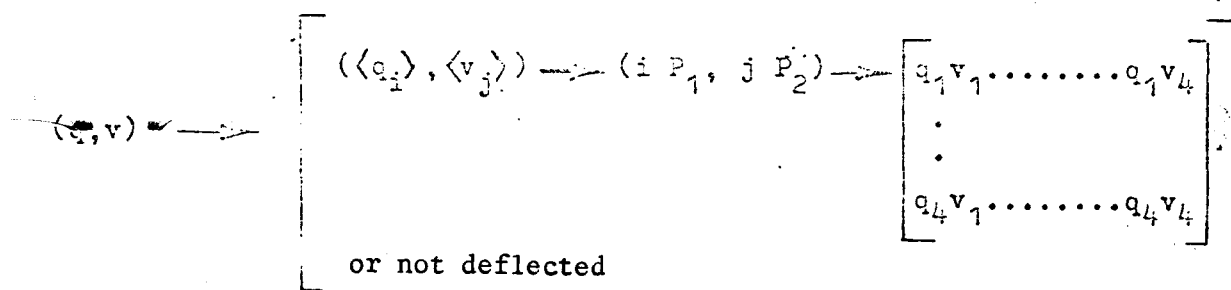
B. The Mass-Velocity Filter

So far it has not been possible to produce dust suitable for acceleration with adequate homogeneity in respect to diameter or mass. Separation methods for homogenizing are extremely complex.

Because of the heterogeneous diameters, and further, because the particles are not exactly spherical, and due to the selective effect of acceleration described in equation (2), the dust accelerator produces a mass-velocity spectrum. Each particle is defined by equation (1) on the basis of its detector signal, but is of arbitrary nature in its (q,v) -value or (m,v) -value. Since it is impossible to assign the detector signals to the craters produced by the particles, the projectiles must be separated after acceleration in order to establish the impact conditions of the craters. This is accomplished by the electrostatic filter [29] described in the following.

In its mechanical portion the filter consists of an arrangement of two crossed plate systems of four deflection condensators P_1 and P_2 each, as shown in Fig. 1. The block wiring diagram is shown in Fig. 2.

Each particle produces two signals in the detectors which uniquely determine the mass and velocity of the particle. These signals are compared with /6 electronically preselected values in the filter. When these agree the particle is deflected at the deflecting plates by high voltage impulses while still in flight, that is into one of the sixteen impact areas (focal points) of the target. Accordingly, an interval $(\langle q_i \rangle, \langle v_j \rangle)$ and, by connecting $i P_1$ and $j P_2$ pairs of plates, a focal spot matrix (q_i, v_j) are assigned to the (q,v) -value of the particle:



for $i, j = 1, \dots, 4$.

The electronic portion also permits limitation to one particle type. Furthermore, the distances of the focal spots or rather, their position, can be changed within certain limits by varying the amplitude of the high voltage impulses.

The switching rate of the logic portion may amount to 300 nsec. The rise time of the high voltage impulses is about 1 μ sec. Therefore it is in principle possible to analyze particles up to 70 km/sec with reasonable filter dimensions.

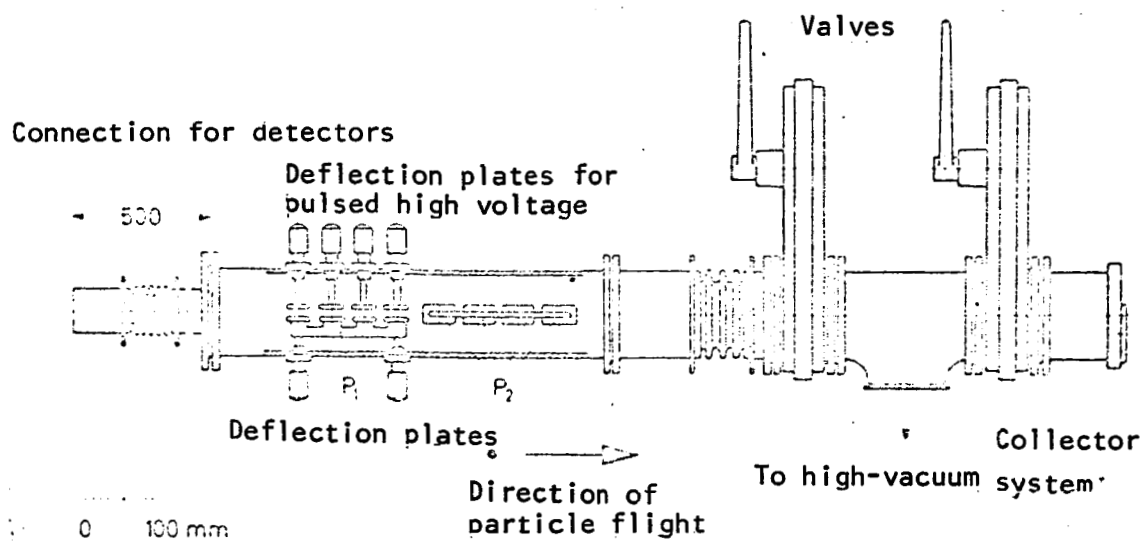


Fig. 1: Assembly Diagram of the Filter

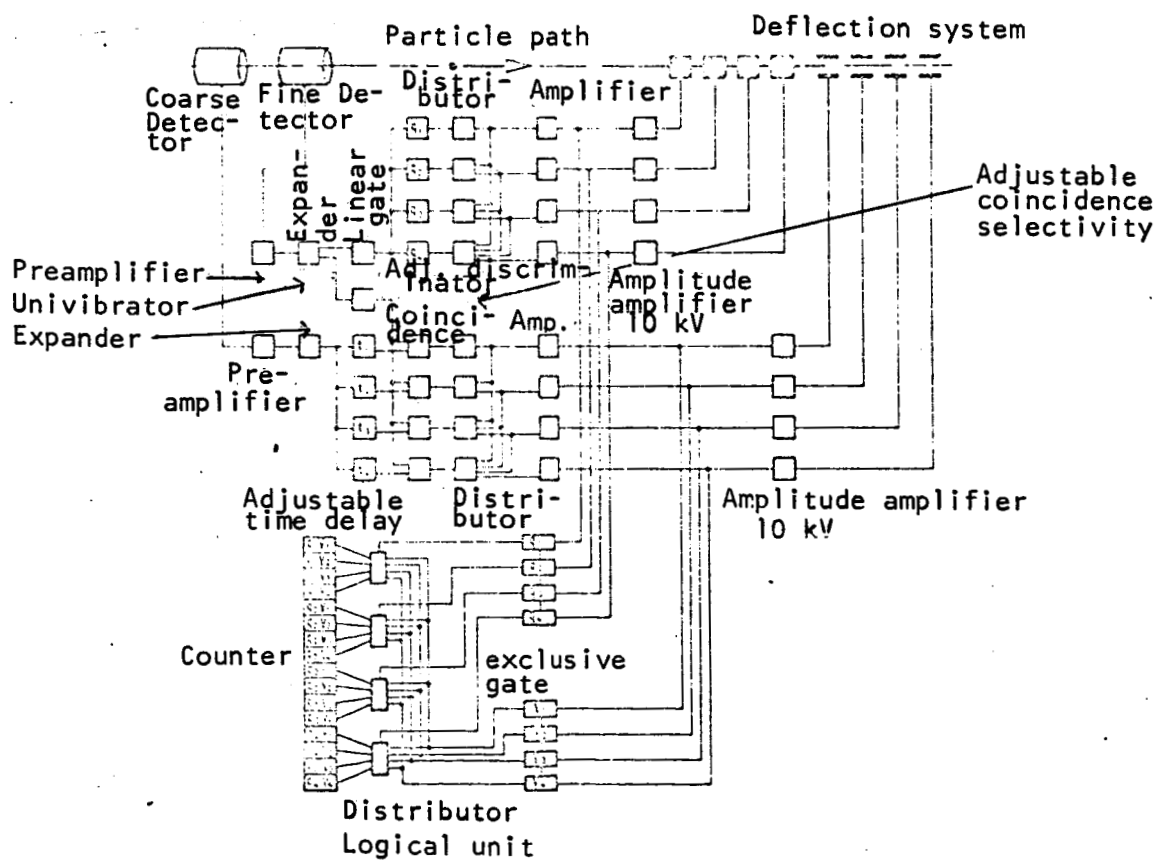


Fig. 2: Block Diagram of the Filter

In detail, the particles are separated as follows: the values (q,v) are /7 taken from the coarse and fine detector. These detectors consist of two cylindrical condensators each. Between these, a crossed pair of plates is provided which can be used for rough determination of the particle path coordinates. Therefore one obtains a complex impulse of the form shown in Fig. 3. After amplifying, the two signals (the input signals of the filter) are expanded to assure satisfactory processing of the pulses. These signals are subsequently converted into impulse peaks with amplitude fidelity to obtain short switching times. These signals are further processed in two separate electronic switch blocks simultaneously.

1. The Velocity Section

The signal of the fine detector lags behind that of the coarse detector because the particle passes first through the coarse and then through the fine detector. The signal of the coarse detector is delayed in four channels, and in coincidences compared with the signal of the fine detector. If the /8 flight time of the projectile within the coincidence width matches one of the four lag times, as for instance that of the j -th channel, then this channel, through the distributor, will actuate j high-voltage square-wave impulses which in turn will actuate the first j deflecting condensators of P_2 and will direct the projectile accordingly.

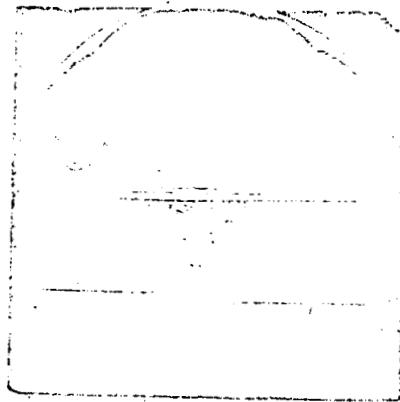


Fig. 3: Shape of the Impulse of the Coarse Detector (above), and the Fine Detector (below).

Each of the four velocity channels can be set for twelve different values. Thus, 12^4 velocity programs can be set up with 48 different velocities. Furthermore, the impulse peak of the fine detector can be extended to 12 different values in order to modify the coincidence width and thus the accuracy of the velocity analysis.

2. The Charging Section.

The charge q of the projectile is determined from the impulse amplitude, simultaneously with the signal of the fine detector which has been expanded with amplitude fidelity. Four window discriminators are available for this purpose, with the position and the width of the windows being continuously variable. When one of the four discriminators reacts, as for instance the i -th discriminator, it actuates the first i pairs of high voltage plates, as in the velocity section. The particle is deflected according to the number of condensers actuated.

3. Registry

When both a charge channel i and a velocity channel j react simultaneously, the counter consisting of 16 channels is actuated through a gate and a distributor, and the event is registered in the channel (q_i, v_j) . In case the channels should cross, the channel with the higher number i, j will have priority, i.e. the particle is deflected into the field with the higher (q_i, v_j) and also registered there.

The logic portion of the filter was checked by electronic comparison of the signals recorded in the counter with the detector signals. The operating effectiveness of the deflecting portion of the filter was confirmed by the uniformity of the craters in one focal spot.

The (q, v) - and the (m, v) -spectrum of carbonyl iron were determined at 1.9 MV by means of the analog portion of the filter. The diameter distribution of this spectrum has a maximum at 2μ and extends from $0.1 - 5\mu$. This spectrum is shown in Fig. 4, together with particle frequencies for the measuring intervals.

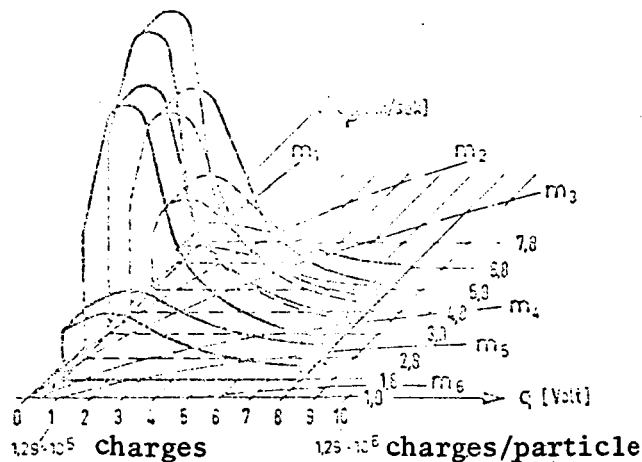


Fig. 4: (q, v) - and (m, v) -Spectrum of Carbonyl Iron Determined by the Logic Portion of the Filter at 1.9 MV.
 q = Particle Charge, v = Particle Velocity.

Table 1:

	Mass m in 10^{-12} g	Radius in μ
m_1	0.88	0.30
m_2	4.4	0.51
m_3	8.8	0.65
m_4	44.0	1.10
m_5	88.0	1.39
m_6	440.0	1.76

C. Absolute Calibration of Projectile Parameters.

/9

Equation (1)

$$m v^2/2 = q U$$

defines the relationship between the projectile constants, mass m , charge q , velocity v , and generator voltage U . These four constants were to be calibrated.

The acceleration voltage U of the band generator, which can be adjusted at equal focusing by means of a short-circuit rod, was calibrated by a Li (p,n)-threshold using a proton source.

The velocity is given by $v = s/t$, where s is the effective distance between coarse- and fine-detector, and t the flight time required to pass through this distance. The effective distance s was determined by electronic comparison with exactly calibrated flight distances [47]. The flight time was determined by electronic counting of the oscillations of a 20 MHz quartz-controlled oscillator. The oscillator was actuated by the impulse rise of the coarse detector and stopped by the rise of the fine detector.

The charge q was calibrated by determining the amplification k of the fine detector amplifier using the calibrated input capacity C of the amplifier, so that in CGS-units

$$q = C E/A$$

where H = impulse amplitude at the amplifier exit.

/10

Calibration of the amplifier resulted in a value for the projectile energy E_p , expressed in MKS-units, of

$$E_p = m v^2/2 = 1.99 \cdot 10^{-14} H U ; \quad (3)$$

it follows that the projectile mass m is

$$m = 3.98 \cdot 10^{-14} H U/v^2 , \quad (4)$$

and since the volume of a sphere is $V_p = d^3 \pi/6$, the projectile diameter d is

$$d = 2.135 \cdot 10^{-4} (H U/v^2)^{1/3} . \quad (5)$$

If m is measured in grams, d in μ , U in MV, H in volts, E_p in erg, and v in km/sec, then

$$E_p = 1,99 \cdot 10^{-11} H U^2, \quad (6)$$

$$n = 3,98 \cdot 10^{-11} H U/v^2 \quad \text{and} \quad (7)$$

$$d = 2,135 (H U/v^2)^{1/3} \quad (8)$$

D. Test Procedures for Evaluation of the Craters.

Because of the smallness of the craters, determination of the crater diameter, and especially of the crater depth by optical microscope is either very inaccurate or entirely impossible.

The micro-craters were therefore evaluated by use of a direct light electron microscope (Stereoscan of Cambridge Co.). In the Stereoscan an electron ray of about 200 Å scans the target point for point, and moves across the target in a line-scanning pattern. The low-energy, secondary electrons produced in the process are accelerated and focused onto a crystal where they produce light pulses. The x,y-deflection of a fluorescent screen is synchronously coupled with the electron scanning velocity. The image produced in this manner is rich in contrast due to the shading effect of uneven surfaces and due to the angle-dependent secondary emission. The image can be photographically recorded.

One exposure perpendicular to the crater is sufficient for determination of the crater diameter; but a second exposure taken from a different angle is necessary to determine the depth.

Model 1:

The image of a crater taken from an angle α is the projection of that crater onto a plane perpendicular to the line of sight, as shown in Fig. 5. Therefore, if P_1 is a point on the target surface outside of the crater, and P_2 a point in the bottom of the crater, we have for $\alpha = 0$: /11

$$\overline{P_1 P_2} = x_0 = x_1 + x_2 \quad (9)$$

and for $\alpha \neq 0$:

$$\overline{P_1 P_2} = x_1' + t' + x_2' = x_0'$$

Since $x_1' = x_1 \cos \alpha$, $x_2' = x_2 \cos \alpha$, and $t' = T \sin \alpha$, it follows that

From equation (9) it follows then that

$$x'_0 = x_0 \cos a + T \sin a \quad \text{or}$$

$$T = (x'_0 - x_0 \cos a) / \sin a \quad (10)$$

Since x'_0 and x_0 can be taken from the pictures of the craters and since a can be measured, the depth T of a point in the bottom of the crater can be found. It is possible in this manner to determine the entire geometry of the interior of the crater (possibly with rotation of the target) provided prominent points exist in the crater and outside on the surface of the target. Where suitable points for measurement could not be found, such points were established by a fixed electron ray. (If the electron ray is left fixed onto the target, a bright spot which roughly corresponds to the diameter of the ray will form after about ten minutes.)

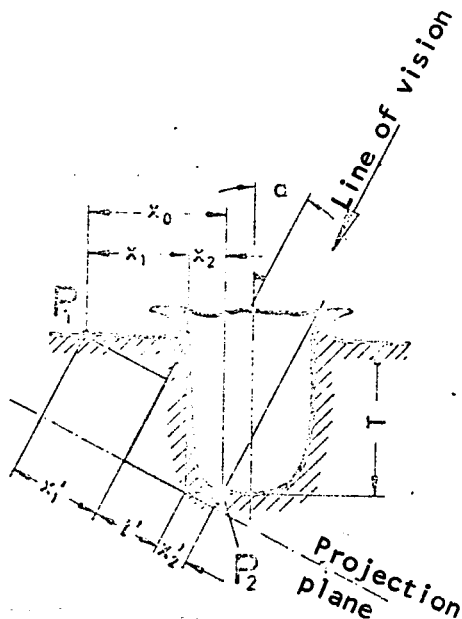


Fig. 5: Cross-Section of a crater for Determination of Depth According to Model 1.

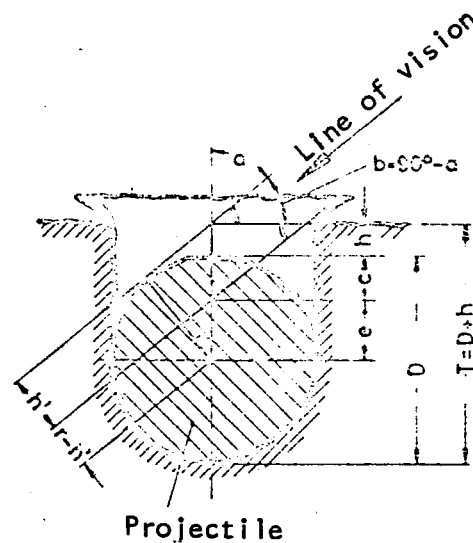


Fig. 6: Cross-Section of a Crater Containing a Projectile, for Determination of Depth According to Model 2.

Model 2:

In the case where an intact projectile body is still present in the crater, the following model was used.

According to Fig. 6, we have:

From $c = D/2 - e$ and $e = (D/2 - h')/\cos b$, it follows that

$$\begin{aligned} h &= \frac{D \tan b}{2} - \frac{D}{2} - \frac{D/2 - h'}{\cos b}, \text{ or} \\ -h &= \frac{h'}{\cos b} + \left(1 - \frac{1}{\cos b} - \tan b\right) \frac{D}{2} \\ &\quad \cos(b) \quad D/2 \quad \text{or} \\ -h &= \frac{h' + (\cos b - \sin b - 1)D/2}{\cos b}, \end{aligned} \quad (11)$$

where the angle $b = 90^\circ - a$.

Because of the height h' for a small crater rim can be measured as the /12 height of the sphere above the crater rim in oblique view, the height h can be determined from h' according to equation (11). With

$$T = D + h \quad (12)$$

this also determines the depth of the crater without projectile body.

This model is also valid in the case where the sphere projects above the surface, provided the depth of penetration is at least $D/2$. The sign of h must then be changed accordingly.

The angle a and the enlargement of the electron microscope were calibrated by means of the incidental light microscope of an optical microscope.

IV. Tests

A. The Testing Range

The following tests were carried out with Fe-projectiles in the (m, v) -range shown in Fig. 4, i.e. with projectiles in the velocity range of 0.5 to 10 km/sec, and with diameters ranging from a few $1/10 \mu$ to several μ . The test range of the projectiles is limited by the distribution of dust diameters, by the acceleration process, and by the size of the craters to be measured.

1.) The lower limit of the smallest projectiles used in the tests is given by the craters produced, because a crater with a diameter smaller than 1μ can presently not be evaluated with sufficient accuracy.

2.) Going toward larger diameters, the projectile diameters are limited by the particle size distribution of the dust. This limit is also dependent on velocity, because acceleration is accompanied by selection as to velocity according to equation (2), i.e. faster particles will on the average have

smaller diameters.

3.) During a constant acceleration period ("radiation period") a varying number of particles will be obtained for equal intervals of $\langle q_i \rangle$, $\langle v_j \rangle$, as evident from the (q,v) -spectrum in Fig. 4. The size of the intervals is determined by the desired measuring accuracy. Toward the margins of the spectrum this results in intervals containing amounts of particles that are so small that /13 they are equal to the amount of random coincidence and do no longer permit reliable measurements.

Most of the random coincidences arise from so called "double particles". When two particles leave the dust source simultaneously and arrive in the detector at different velocities, the first particle will be correctly sorted but the second particle may be directed into the focal point of the first particle because the voltage actuated by the first particle is applied to the deflecting plate for about 1 msec. About 2 - 3% of the particles will be incorrectly deflected. Therefore several craters are required in one focal spot as a check. (Furthermore, a single crater, and especially a single small crater, is difficult to find in a focal spot which has a diameter of about 3 - 4 mm.)

In the tests the intervals $\langle q \rangle$ and $\langle v \rangle$ were therefore generally chosen such that their width was equal to $\pm 5\%$ of the average value of the intervals. Furthermore, only those projectiles were used for which the rate per interval per hour was at least 30.

B. General Appearance of the Craters.

Craters were produced and measured in Pb, Cd, Cu, Ag, Ni, Ti, Be and Au, and the first five materials were systematically investigated. The following general appearance was found: the classification by crater characteristics given in chapter II for the crater tests with cm-projectiles, into the velocity ranges A (projectile intact), B (transition), and C (liquid impact), appears reasonable for the μ -projectiles as well. For instance, Fig. 7a shows the impact of Fe-projectiles on a Cu-target (denoted by the symbol Fe \rightarrow Cu). At a projectile velocity of $v = 0.5$ km/sec the projectile lies shattered in the bottom of the crater; at $v = 5.2$ km/sec the projectile can no longer be recognized, but the bottom of the crater does still contain iron as could be determined by x-ray microanalysis [5] using a counting tube mounted on the Steroscan and a multi-channel analyzer. At low velocities the projectile remains intact, but it deforms more and more with increasing velocity. At velocities in excess of about 4 km/sec, the remainder of the particle is undistinguishably mixed with the walls of the crater.

At velocities greater than 1 km/sec, the craters have a typically fractured rim, below this velocity the rim becomes smaller and disappears completely, for aluminum for instance at a velocity of 0.5 km/sec (Fig. 7b). Because of its /16 irregularity, it is difficult to measure the outer diameter of the crater rim. Within the accuracy of measurement, the average outside diameter D_a of the rim is, at velocities of more than 1 km/sec and for all materials investigated, proportional to the interior diameter of the crater with the same constant of

proportionality, as indicated in Fig. 8. For this reason, and because the interior diameter of the craters can be measured much more accurately, only the interior diameter D will be used in the following.

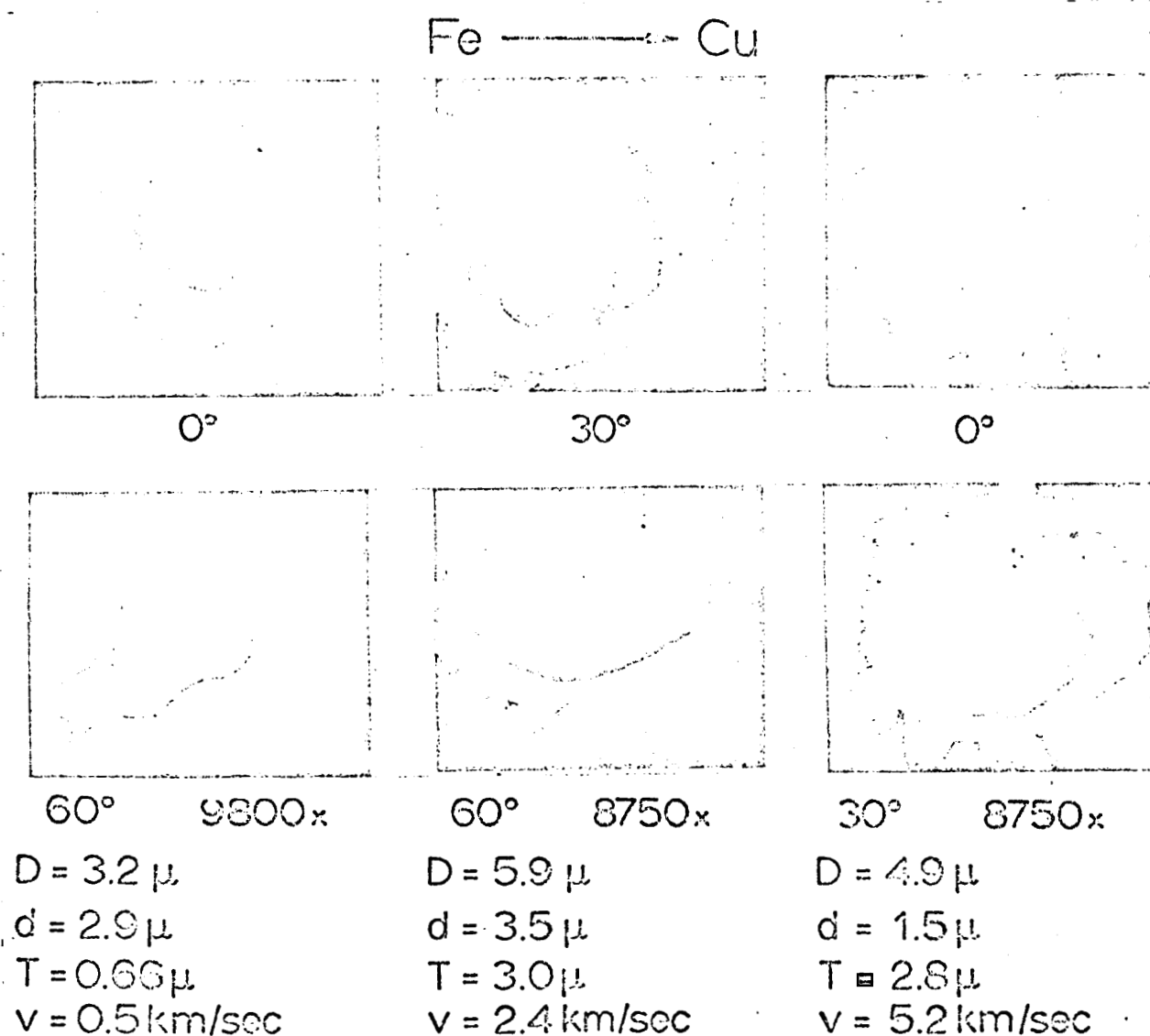
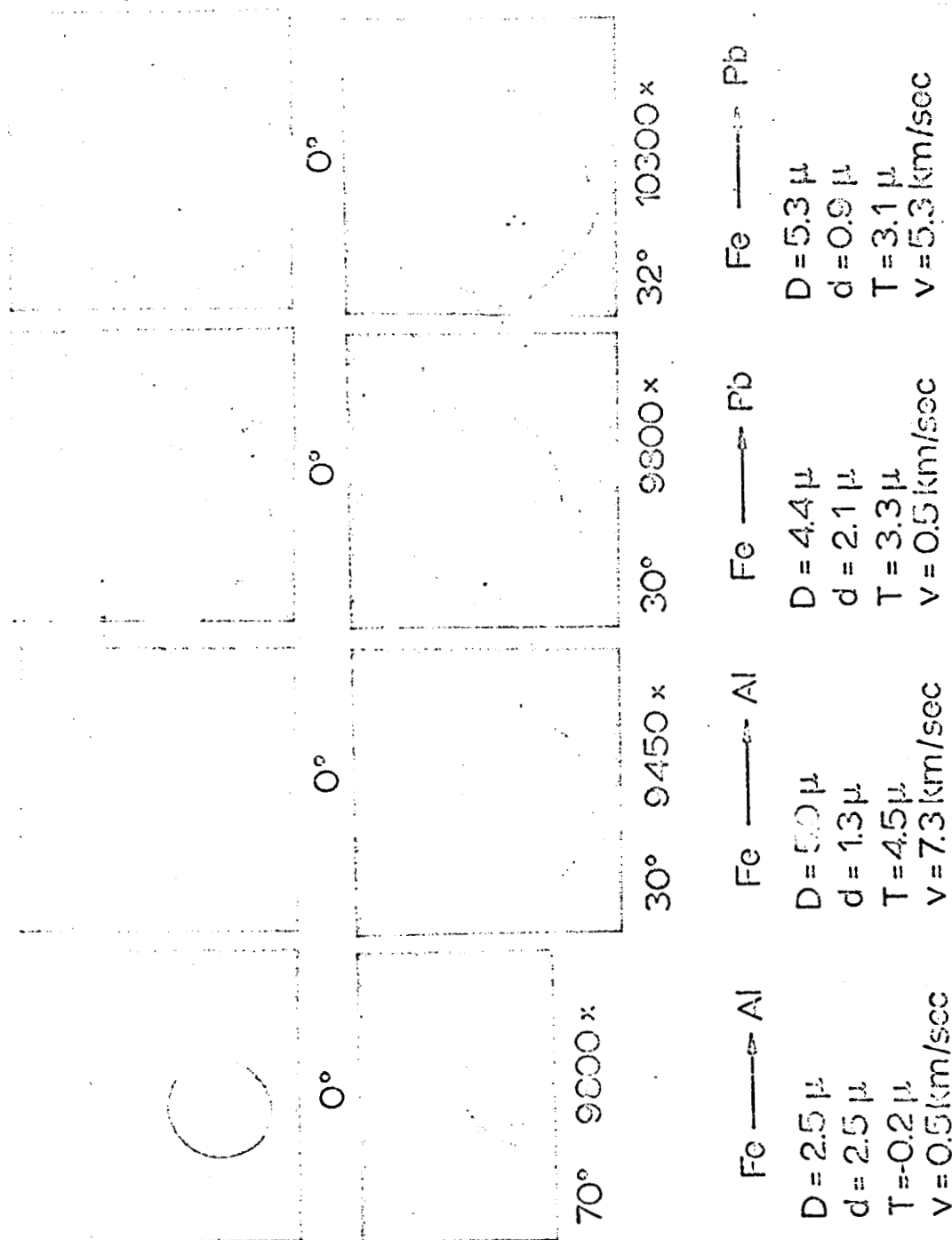


Fig. 7a: Shape of Cu-Craters Seen From Different Angles, for Projectile Velocities of $v = 0.5$ km/sec, $v = 2.4$ km/sec, and $v = 5.2$ km/sec. At $v = 0.5$ km/sec the projectile is almost unaltered, at $v = 2.4$ km/sec it is destroyed, and at 5.2 km/sec it can no longer be recognized. (But Fe can still be found).

/14



Eig. 7b: Left: Shape of Al-Craters Seen From Different Angles, For Projectile /15
Velocities of $v = 0.5$ km/sec and $v = 7.3$ km/sec.
Right: Shape of Pb-Craters for $v = 0.5$ km/sec and $v = 5.3$ km/sec.
At 0.5 km/sec the nearly unaltered projectile is visible in the crater for both materials.

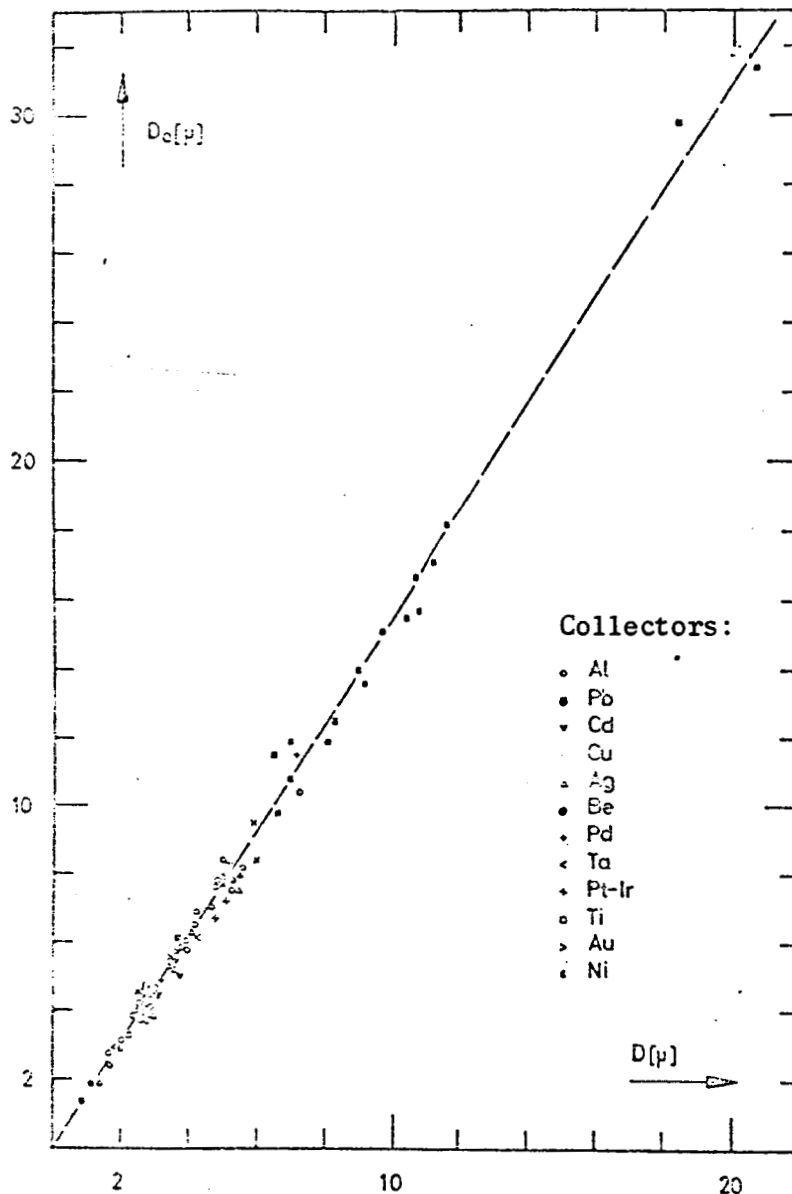


Fig. 8: Outside Diameter D_o of a Crater as a Function of the Interior Diameter D of the Crater, for Varying Projectile Velocities $v > 1$ km/sec, and for Different Materials.

Since the entire deformed or shattered projectile may be present in the crater, but only the "visible" crater bottom (i.e. either the surface above the projectile, the surface above the remainder of the projectile, or the surface above the "actual" crater bottom) is capable of measurement, it is at first possible to find only the "visible" depth, as indicated in Fig. 9. Visible depth may be defined as the distance from the undisturbed surface of the target ^{/17} to the center of the visible crater bottom. The actual depth T' of the crater is not capable of measurement but it can be approximated by use of a mathematical

model.

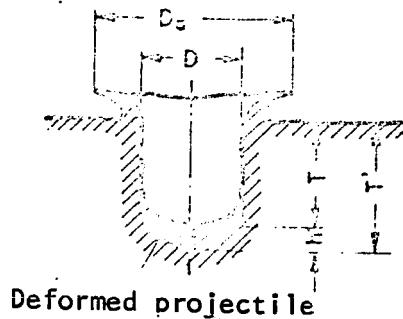


Fig. 9: Cross-Section Through A Crater, for Definition of Symbols:

D_a = Average Outside Diameter

D = Inside Diameter

T = Visible Depth

T' = Actual Depth

h = Average Height of Deformed Projectile

The undisturbed target surface can easily be measured since it is altered only in the immediate vicinity of the craters. The surface is even with a roughness that is generally less than 0.05μ . The target surface of the several mm thick target plates was finished by vibration-polishing in several passes, using consecutively finer-grained diamond paste. An exception are the Pb-targets which could not be polished in this manner because of the softness of the material and which were cut by ultramicrotome. The roughness obtained was about $1/10 \mu$. The target surfaces consist of pure materials.

C. Crater Diameter

The crater diameter for perpendicular impact depends on the projectile diameter d , the projectile velocity v , and on the target material (the projectile mass is iron); therefore

$$D = f(v, d, \text{Targetmaterial}) . \quad (13)$$

It is important here that one or more values be isolated. It is to be expected that laws of similarity will apply for different projectile diameters. The simplest relationship of this type is expressed by

$$D = c_1 d , \quad (14)$$

where $v = \text{const.}$ and c_1 depends on the material. The tests shown in Figs. 10 through 14 confirm this assumption within the accuracy of measurement. Figs. 10 and 11 show this relationship for the target material Al; the projectile velocity was $v = 4.15 \pm 0.15 \text{ km/sec}$ for Fig. 10, and $v = 5.15 \pm 0.15 \text{ km/sec}$ for Fig. 11. Comparison of the two figures shows that equation (14) is dependent on velocity. Figs. 12, 13, and 14 show the proportionality for Cu, Ag and Cd, respectively, at a velocity of $v = 4.0 \pm 0.1 \text{ km/sec}$. Figs. 10 through 14 show that the value of equation (14) for equal projectile velocities depends on the material, i.e. c_1 is a material constant.

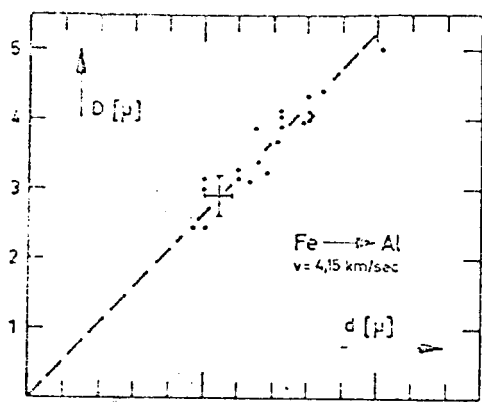


Fig. 10

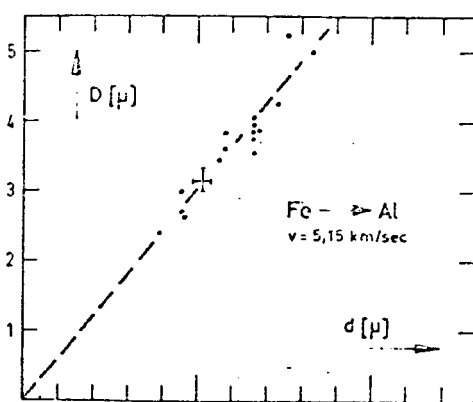


Fig. 11

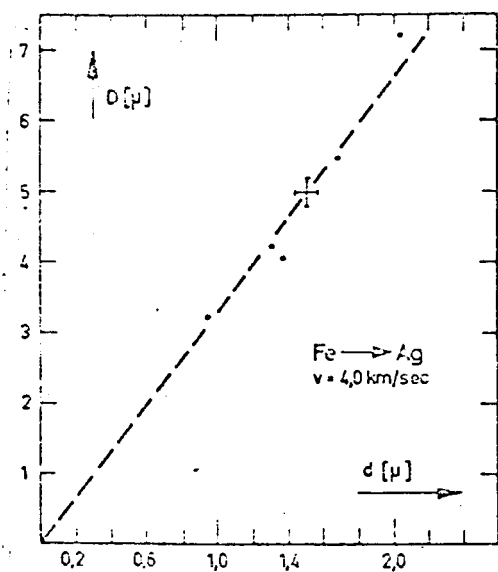


Fig. 12

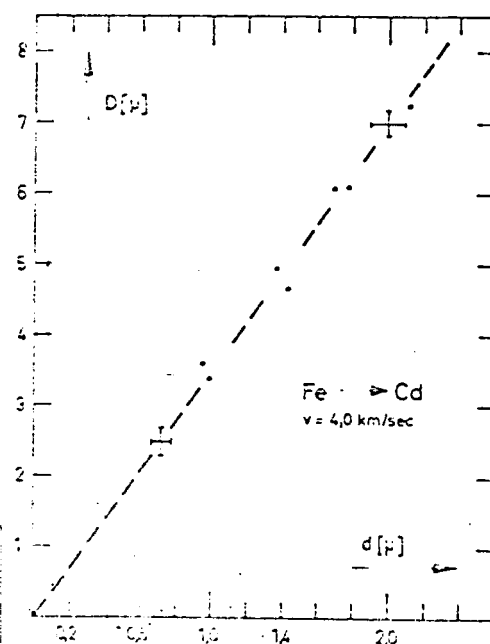


Fig. 14

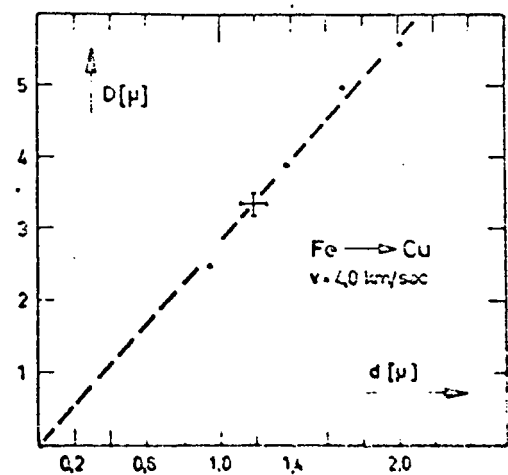


Fig. 13

Figs. 10 through 14: The Crater Diameter D as a Function of the Projectile Diameter d , For Varying Projectile Mass. /18

- Fig. 10: Fe→Al, $v = 4.15 \pm 0.15$ km/sec
 Fig. 11: Fe→Al, $v = 5.15 \pm 0.15$ km/sec
 Fig. 12: Fe→Ag, $v = 4.0 \pm 0.1$ km/sec
 Fig. 13: Fe→Cu, $v = 4.0 \pm 0.1$ km/sec
 Fig. 14: Fe→Cd, $v = 4.0 \pm 0.1$ km/sec

Therefore equation (14) can be written in the form of a similarity equation with respect to the projectile diameter: /19

$$D/d = g(v, \text{Material}) . \quad (15)$$

Figs. 15 - 19 show this relationship for firm target materials Al, Cu, Ag, Cd, and Pb. The curves can be expressed by

$$D/d = c_2 S(v) \quad (16)$$

where c_2 is a constant that depends on the type of material. For Al and Cu (Figs. 15 and 16) at low velocity, the crater diameter corresponds roughly to the projectile diameter. Then, at constant projectile diameter, the crater diameter increases with increasing velocity. This is also true for the other materials Ag, Cd, and Pb (Figs. 17-19). Written in exponential form, the /20
equation

$$D/d = c_2 v^{2/3} \quad (17)$$

describes the shape of the curves for higher velocities. In the case of Cd (see Fig. 18) the ratio D/d varies with a somewhat higher exponent of velocity; but this may be due to an insufficient number of test points.

Since the crater diameter at speeds faster than 1 km/sec increases with increasing velocity as the projectiles get smaller (see discussion on page 18), and due to the given dust particle distribution, the crater diameter distribution shown in Fig. 20 is obtained for Al, expressed as a function of projectile velocity. The projectile velocity taken from the curve in Fig. 15 has been used as a parameter in constructing this diagram. The dashed line at $D = 1 \mu$ shows the limit of measurement due to the resolving power of the Stereoscan apparatus. As shown, Al-craters cannot be evaluated at velocities in excess of 11 km/sec. The points shown in Fig. 20 represent all Al-craters measured. Accordingly, all Al-curves are based on this range and are rigorously valid only within that range.

D. Measurable Crater Depth and Crater Shape.

Crater depth is a function of the target material, of the projectile velocity v and the projectile diameter d , and has the general form

(18)

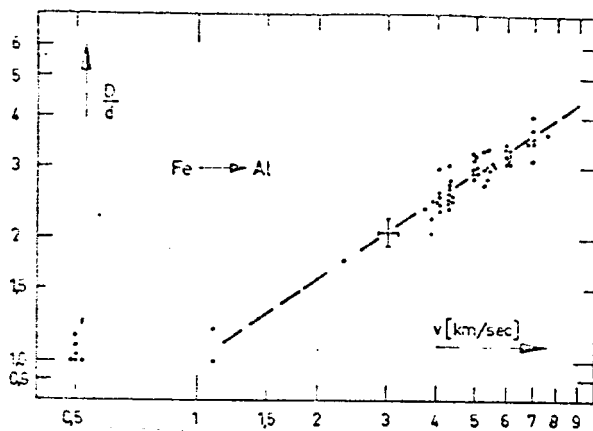


Fig. 15

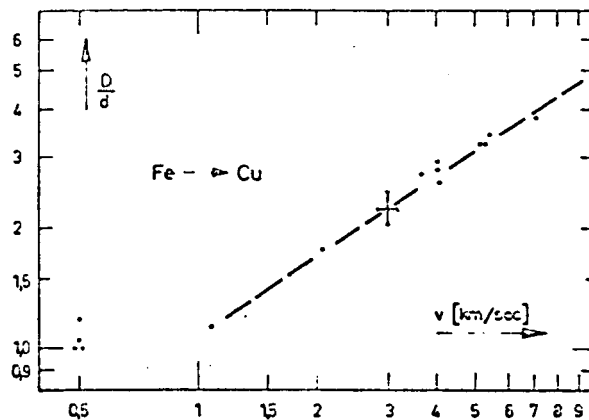


Fig. 16

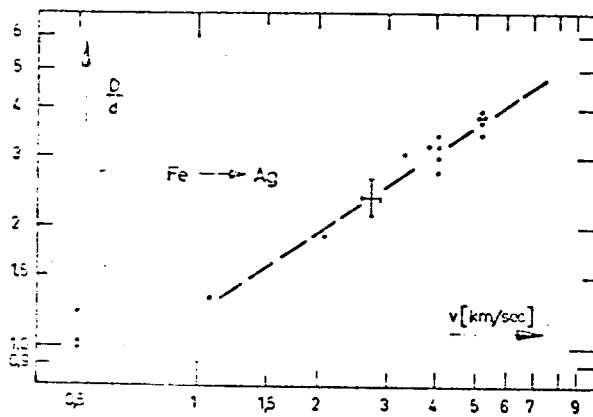


Fig. 17

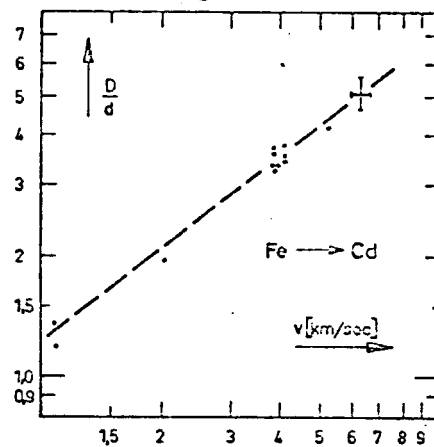


Fig. 18

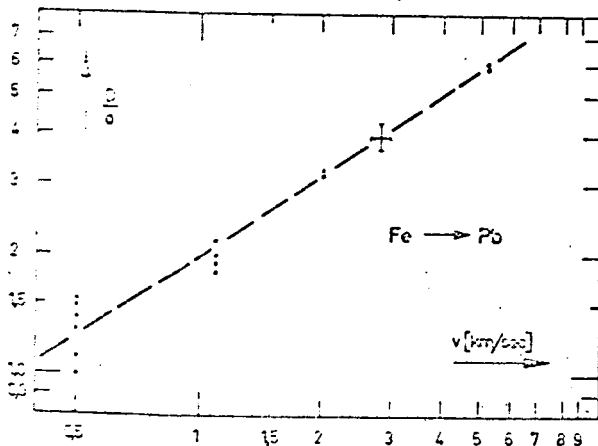


Fig. 19

Fig. 15 - 19: Ratio of Crater Diameter to Projectile Diameter D/d Expressed as a Function of the Projectile Velocity v for Different Target Materials, i.e. in Fig. 15 for Al, in Fig. 16 for Cu, in Fig. 17 for Ag, in Fig. 18 for Cd, and in Fig. 19 for Pb.

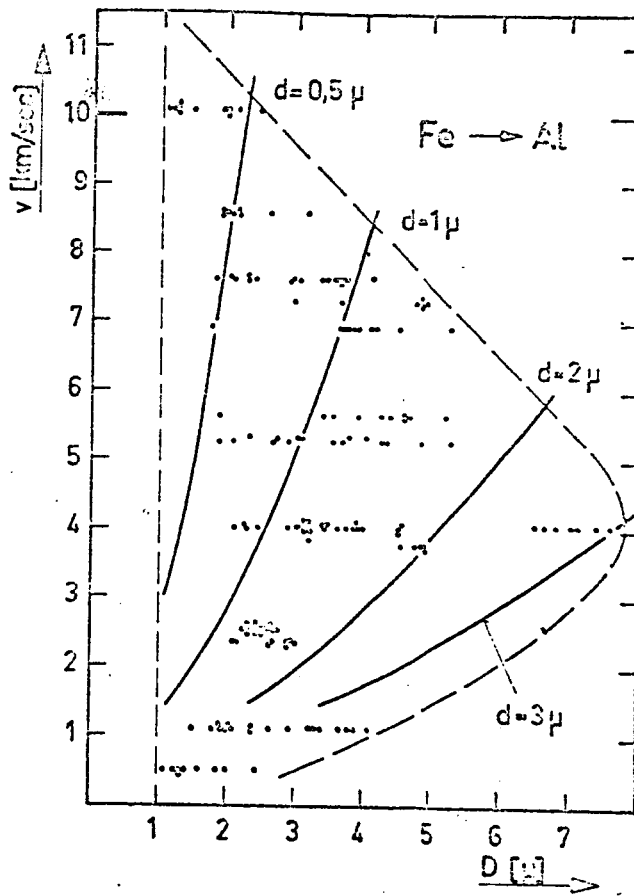


Fig. 20: Relationship Between Crater Diameter D and Projectile Velocity v for Al-Targets (Range Investigated).

Laws of similarity may be expected as in the case of the crater diameter. /21
Here, the crater shape is similar at constant projectile velocity. Therefore

$$T = D G(v, \text{Targetmaterial}) . \quad (19)$$

for $v = \text{constant}$, and for the same target material

$$T = \text{const. } D . \quad (20)$$

This equation is confirmed by Figs. 21-24, for instance by Fig. 21 at $v = 4.0 \pm 0.1$ km/sec, and by Fig. 22 for Al at $v = 7.6 \pm 0.3$ km/sec. In Fig. 23 this is confirmed for Ag at $v = 4.0 \pm 0.1$ km/sec, and in Fig. 24 for Cd at $v = 2.5 \pm 0.1$ km/sec. These curves are representative of a large number of curves that are not shown, so that equation (20) is valid for the range investigated within the

accuracy of measurement.

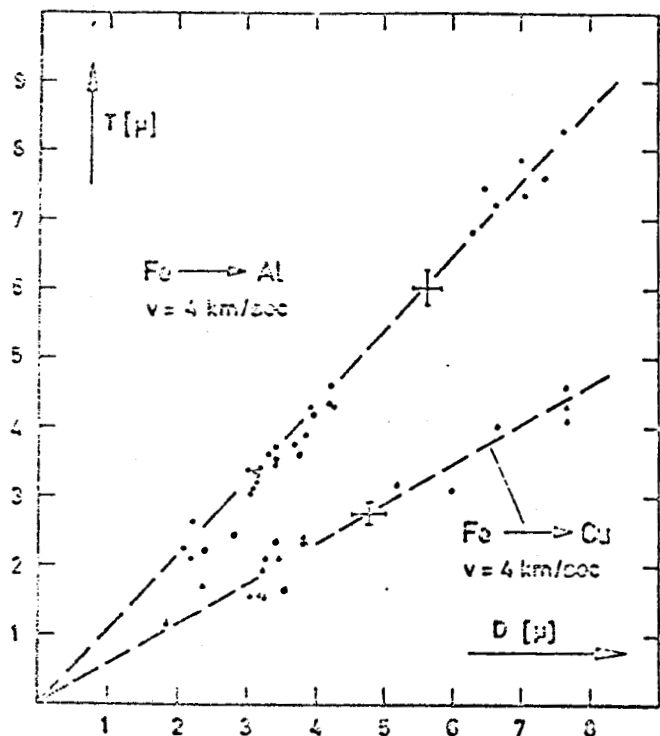


Fig. 21

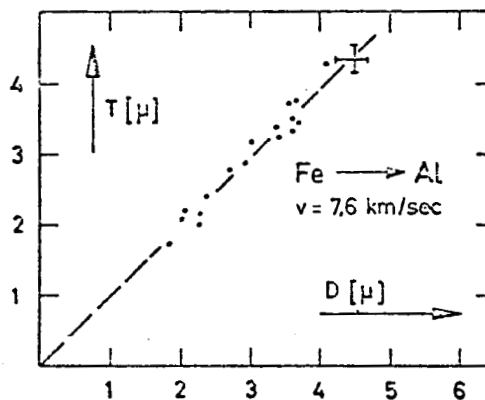


Fig. 22

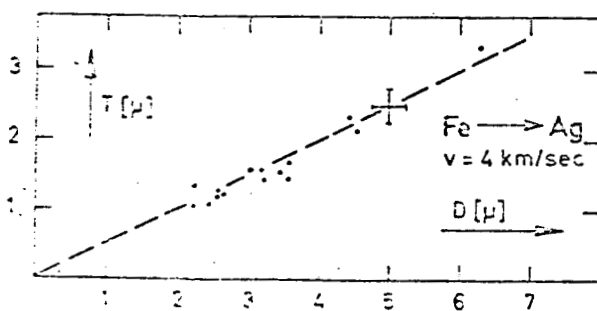


Fig. 23

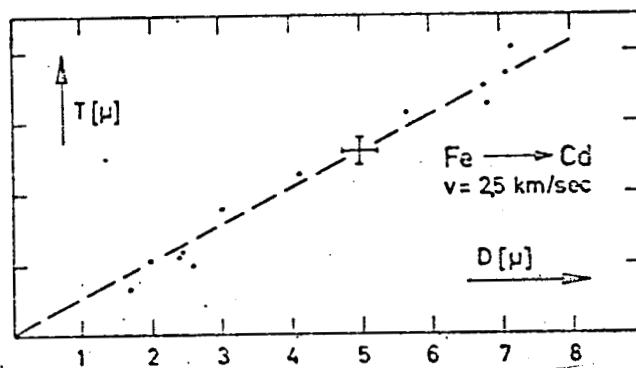


Fig. 24

Figs. 21 - 24: Measurable Crater Depth T as a Function of the Crater Diameter D , for Varying Mass.

Fig. 21: Al- and Cu-target, $v = 4.0 \pm 0.1$ km/sec;

Fig. 22: Al-target, $v = 7.6 \pm 0.3$ km/sec,

Fig. 23: Ag-target, $v = 4.0 \pm 0.1$ km/sec,

Fig. 24: Cd-target, $v = 2.5 \pm 0.1$ km/sec.

From equation (19) the shape factor T/D is solely a function of projectile velocity and target material:

$$T/D = G(v, \text{target material}). \quad (21)$$

Figs. 25 - 27 show the curves for Al, Cd, Ag, Cu and Pb. At low velocities, up to about 2 km/sec, the craters show a wider scattering of the shape factor, which cannot be explained by inaccuracy in measurement alone. In this range the curves are also different for the individual materials. For velocities of roughly more than 3 km/sec the crater shapes are rigorously similar for the same material and are independent of velocity. The curves are given by the equation /22

$$T/D = c_3 \quad (22)$$

where c_3 is a value that depends on the material, i.e. for greater velocity the function given by equation (19) reduces to the material - dependent constant c_3 . However, since the crater diameter in this range is given by equation (17), the measureable crater depth is given by

$$T = c_2 c_3 v^{2/3} d = c_4 d v^{2/3} \quad (24)$$

where c_4 is a material constant.

E. The Actual Crater Depth T' /23

The actual crater depth T' (Fig. 9) is the depth without projectile or projectile remainder in the crater. It cannot be measured because the projectile or its remainder cannot be removed due to the smallness of the craters. But the depth T' can be estimated.

Assuming that the entire volume of the projectile is present in the crater and that the shape of the projectile is preserved or deformed into an ellipse of rotation with the crater diameter D as diameter and the crater axis as axis of symmetry (Fig. 30), the average height h of the deformed projectile is given by

$$d^3 \pi/6 = D^2 h \pi/6 \quad \text{or} \quad h = d^3/D^2 \quad (25)$$

The projectile diameter d can be determined from the measured values by the use of equation (8), so that

$$(26)$$

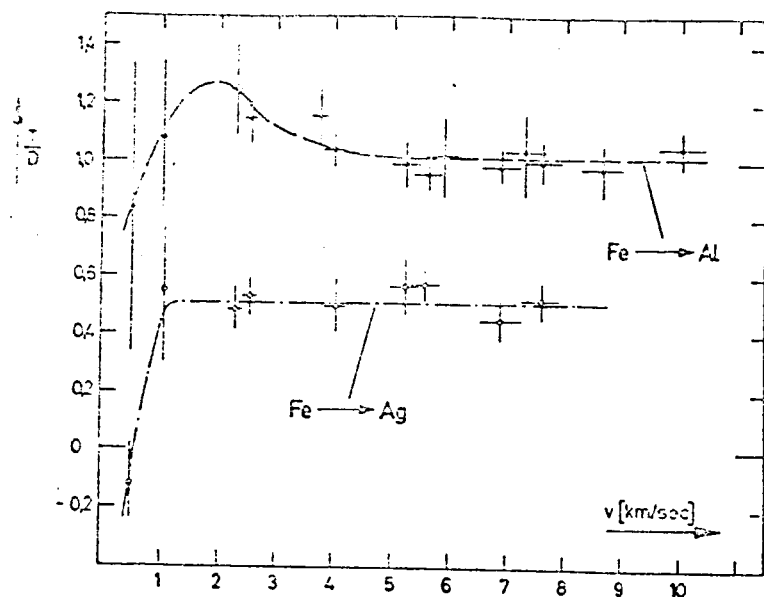


Fig. 25: Al- and Ag-target;
Fig. 26: Pb- and Cd-target;
Fig. 27: Cu-target.

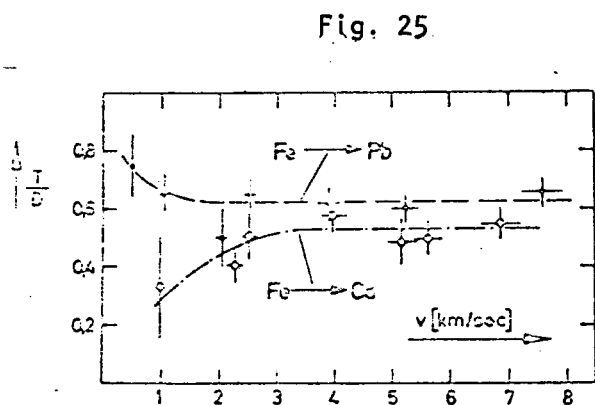


Fig. 26

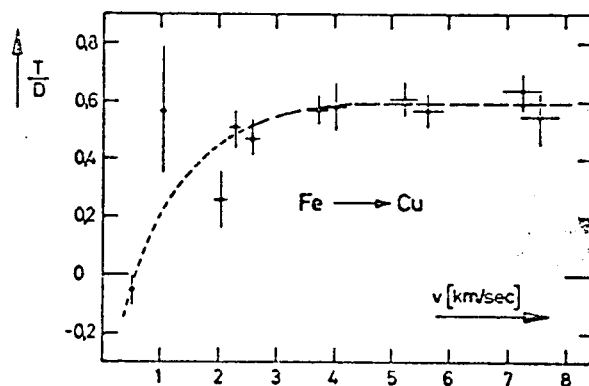


Fig. 27

Figs. 25 - 27: Ratio of Measureable Crater Depth T to Crater Diameter D as a Function of Projectile Velocity v for Varying Mass.

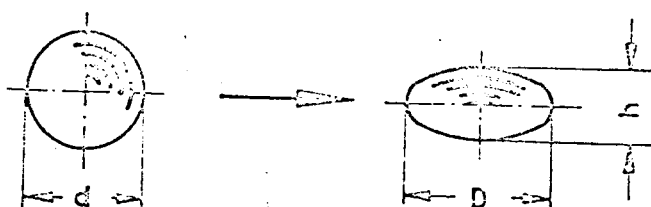


Fig. 30: Cross-Section Through Intact and Deformed Projectiles According to the Mathematical Model for Determination of the Actual Depth T' .

However, the depth T' is approximately given by (see Fig. 9)

$$\begin{aligned} T' &= T + h & \text{or by} \\ T'/D &= T/D + h/D \end{aligned} \quad (27)$$

Equation (17) $D/d = c_2 v^{2/3}$ defines the relationship of the crater diameters for sufficiently high velocities. It follows that

$$T'/D = T/D + 1/(c_2^3 v^2) \quad (28)$$

This indicates that with increasing velocity the "actual" shape factor T'/D rapidly approaches the measureable shape factor, and that the actual crater depth T' approaches the measureable depth T . Using equation (26) and the measured points from Figs. 25-27, the relationship of the actual shape factor and the projectile velocity v is shown in Figs. 31-33. As in Figs. 25-27, the error is taken as the mean square deviation. Fig. 41a shows the true scattering /24 of the test points for aluminum.

F. Crater Volume.

The measureable volume $V(T)$ above the visible bottom can be measured as crater volume. But the "actual" crater volume $V(T')$ without projectile mass is physically more interesting. Assuming that the entire projectile volume V_p is present in the crater, we have

$$V(T') = V(T) + V_p \quad (29)$$

The volume of the projectile is determined from the filter values using equation (7). From equation (29) it follows that

$$V(T')/V_p = V(T)/V_p + 1 \quad (30)$$

Fig. 36 shows the relationship of $V(T')/V_p$ as a function of the projectile /25 velocity v for Pb, Al and Cu. The straight lines shown in the diagram have a slope of 2, i.e. the equation defining this relationship is, within the accuracy of measurement, of the form

$$V(T')/V_p = c_5 v^2 \quad (31)$$

where c_5 is a material constant.

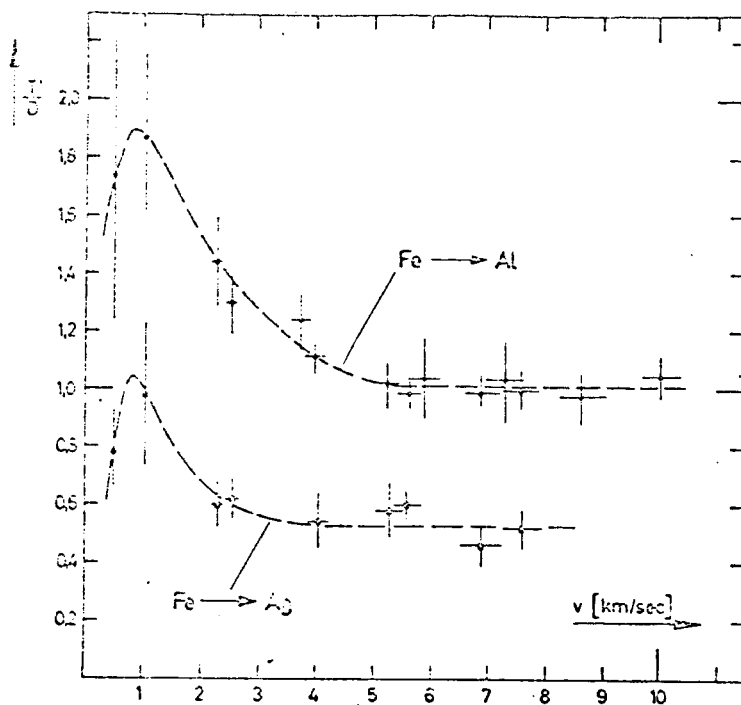


Fig. 31

Fig. 31: Al- and Ag-target;

Fig. 32: Cu- and Cd-target;

Fig. 33: Pb-target.

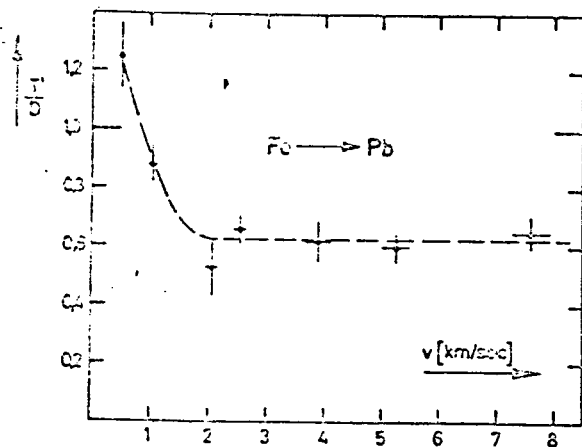


Fig. 33

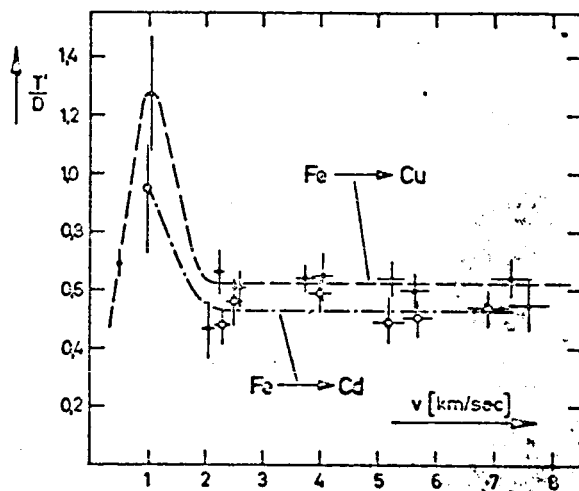


Fig. 32

Figs. 31 - 33: Ratio of Actual Crater Depth T' to Crater Diameter D as a Function of Projectile Velocity v for Varying Mass.

Since the mass m of the projectile is $m = \rho_p V_p$, where ρ_p = density of the projectile, it follows from equation (31) that

(32)

where c_6 is a material constant. This indicates that the crater volume $V(T')$ depends on the material and is proportional to the kinetic energy E_p of the projectile.

The test data for aluminum of Fig. 36 are shown in Fig. 37 in the form of crater volume $V(T')$ as function of the kinetic energy E_p . It should here be noted that the individual test points correspond to different projectile velocities and different projectile masses. The straight line with the slope of 1 shown in this Figure confirms very well the relationship $V(T') = c_6 E_p$ defined by equation (32).

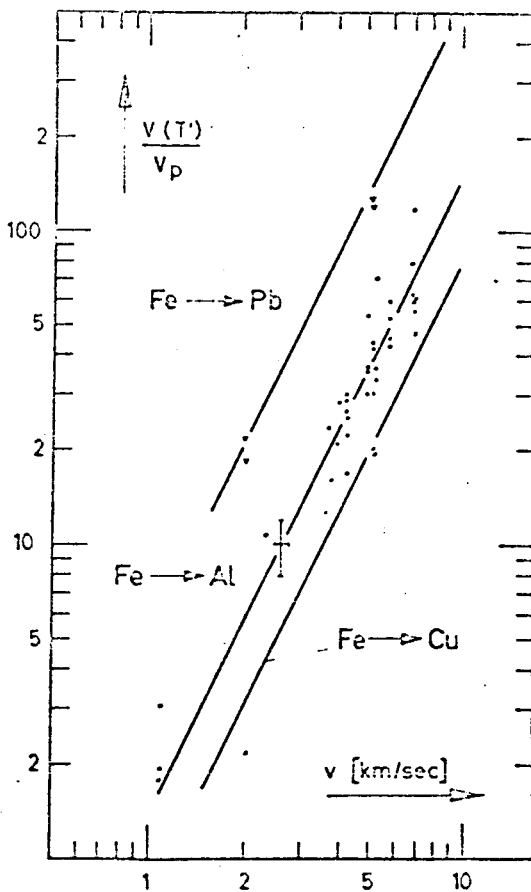


Fig. 36: Ratio of Actual Crater Volume $V(T')$ to Projectile Volume V_p as a Function of Projectile Velocity v , for Varying Projectile Mass. Target Materials are Pb, Al and Cu.

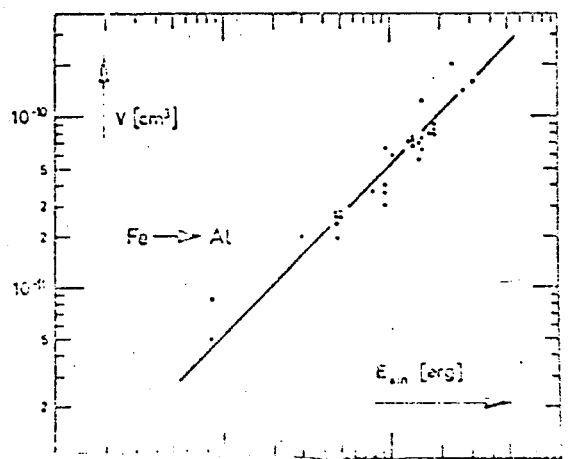


Fig. 37: Actual Crater Volume $V(T')$ of Al-Craters as a Function of Projectile Energy, for Varying Projectile Mass and Varying Projectile Velocity v , where $v \geq 1$ km/sec.

A usable model is needed to understand the test results reported in the preceding chapter.

The dependence on material of the crater values expressed as a function of the test conditions can be reasonably represented only by the use of such a model. Because of the large number of possible target and projectile parameters, the question arises which combinations of parameters are suitable to describe the craters. For instance, the crater diameter D can be represented as a smooth curve by the sonic velocity v_s (energy transport velocity), namely by

$$D = c_7 v_s^{-1/2} \quad (33)$$

where the crater diameter d and the projectile velocity v are constant.

The two straight lines with a slope of $-1/2$ in Fig. 38 show this relationship for Pb, Au, Cd, Al, Ni, Ti and Be. For the upper straight line $d = 1.7 \mu$ and $v = 4.6 \text{ km/sec}$; for the lower straight line $d = 0.91 \mu$ and $v = 5.2 \text{ km/sec}$.

However, smooth curves are not obtained, when crater volume and crater depth are defined in terms of the sonic velocity. Furthermore, no relationship to the sonic velocity of the target can be found for the test curves D/d , T/D , T'/D and $V(T')/V_p$ expressed as function of v .

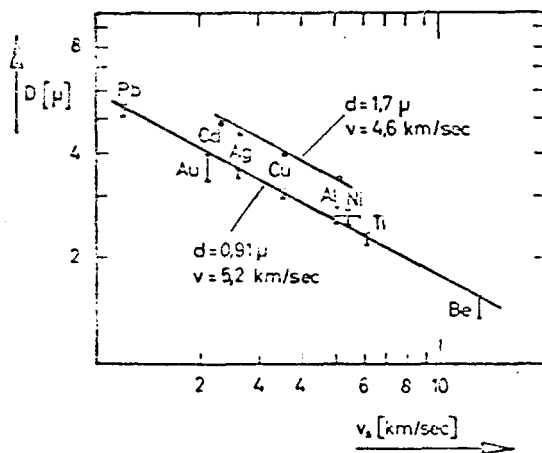


Fig. 38: Crater Diameter D as A Function of the Sonic Velocity v_s of the Target, for Different Target Materials. The Projectile Parameters are Constant for a Particular Straight Line; for the Upper Straight Line: Projectile Diameter $d = 1.7 \mu$, and Projectile Velocity $v = 4.6 \text{ km/sec}$; for the Lower S-aight Line $d = 0.91 \mu$ and $v = 5.2 \text{ km/sec}$.

A. Model Concept.

The formation of craters and the accompanying phenomena constitute a difficult shock wave problem. However, complex processes can be partially described by substitute processes which give an equivalent description of one or more parts of the problem. The question of energy transformation is one of the important partial problems.

As previously discussed, the projectile energy is consumed in a number of simultaneous or sequential processes. Crater formation will now be considered as the main process, and all other phenomena will be

considered as accompanying processes. Examples of this kind are: the emission of ions and electrons, the emission of light, heat radiation, transport of material, and heat conduction. The emission of light and ions and electrons, and heat radiation are negligible in energy considerations because of their small energy requirements.

For the transformation of the energy necessary to form the crater volume in metal surfaces, such substitute process can be stated analogous to the observation made by Furth and Born [49,9]: "melting being nothing else than breaking due to the action of the heat of the atoms; or putting it the other way round, breaking is nothing else than melting enforced by the action of the stress". The analogy lies in the fact that in order to form the crater volume (disregarding the accompanying processes) the projectile must provide energy corresponding to the melting energy.

It is assumed that the energy flow provided by the projectile always flows first through the melting process (breakdown of the lattice structure), then the accompanying processes are sequential processes in the sense that the crater formation proceeds as if the entire projectile energy were solely used to form the crater volume. The accompanying processes can then be considered separately. They satisfy their energy requirements from the latent energy in the crater volume.

Conversely, if the accompanying processes are not subsequent processes in this sense, then one obtains an upper limit for the crater volume (if the entire projectile energy is set equal to the melting energy). The following mathematical model should be understood in this sense.

For the following considerations it is necessary to divide the velocity range of the projectile into two ranges, the range D above the yield point of the projectile, and the range E below the yield point.

1.) The Velocity Range D above the Yield Point of the Projectile.

Let this range be defined by the projectile energy E_p being larger than the melting energy $E(L_p)$ of the projectile,

$$E_p > E(L_p) \quad (34)$$

The melting energy $E(L_p)$ is the sum of two quantities of heat, the amount of heat $E(l_p)$ that is necessary to heat the projectile from 20°C to the melting temperature, and the melting heat $E(L'_p)$. Therefore

$$(35)$$

/28

where L'_p is the melting heat per gram, and l_p the amount of heat per gram needed to raise the temperature.

Equation (34) also defines a critical velocity v_1 . From

$$E_p = \pi v^2/2 > m L_p = m \dot{v}_1^2/2 \quad (36)$$

the critical velocity v_1 is found to be

$$v_1 = (2 L_p)^{1/2} . \quad (37)$$

For metal projectiles this value corresponds to a velocity of roughly 1 km/sec.

2.) The Velocity Range E Below the Yield Point of the Projectile.

Let this range be defined by the projectile energy being insufficient to melt the entire projectile, or

$$E_p < E(L_p) = m L_p . \quad (38)$$

Toward high velocities this range is limited by v_1 on account of equation (37).

For reasons of test procedures let the velocity range be limited toward low velocities by a velocity v_2 determined by the craters formed by the projectile.

In this velocity range, $v_2 \leq v < v_1$, let the crater diameters be

$$D \geq d \text{ sein.} \quad (39)$$

B. The Velocity Range D above the Yield Point of the Projectile.

According to the preceding considerations, the maximum energy $E(L_t)$ that is available to form the crater in the velocity range D is equal to the projectile energy E_p less the melting energy of the projectile, or

$$E(L_t) = E_p - E(L_p) , \quad (40)$$

wherein it is assumed that the projectile melts as well. The energy $E(L_t)$ is the sum of the energy $E(l_t)$ that is required to raise the temperature of the

crater volume by ΔT to the melting point of the target, plus the melting heat $E(L'_t)$ of the crater volume; i.e.

$$E(L_t) = E(l_t) + E(L'_t) \quad (41)$$

Herein, $E(l_t)$ is approximately

$$E(l_t) = \bar{c}_p m_t \Delta T = m_t l_t, \quad (42)$$

where \bar{c}_p is the average specific heat (at constant pressure), m_t the mass of /29 the crater volume, and l_t the amount of heat per gram corresponding to the melting heat $E(l_t)$.

1.) The Crater Diameter

In the case where the crater diameter D is formed by the spreading, molten projectile, and the process ends as the projectile solidifies (at this moment it is exactly at melting temperature), we have

$$E(L_t) = E_p - E(l_p). \quad (43)$$

Here $E(l_p)$ is approximately $E(l_p) = \bar{c}_p m \Delta T$ analogous to equation (42). For craters of semi-ellipsoidal shape, as is the case for most of the craters investigated, the volume is

$$V(T) = D^2 T \pi/6, \quad (44)$$

where D is the crater diameter and T the crater depth. It is now assumed that the crater shape for a particular projectile-target combination is similar and independent of velocity and projectile mass. (This assumption is confirmed for sufficiently high velocities, refer to Figs. 31 - 33). Using a new symbol for depth, T° , we then have

$$T^\circ/D = k, \quad (45)$$

where k is a material constant. If the projectile is a sphere, its volume V_p is defined by the diameter d , or

$$(46)$$

From equations (43) through (46), and from $m = \rho V$ (m = mass, ρ = density) it follows that

$$\rho_t D^2 T^\circ L_t \pi/6 = \rho_p d^3 v^2 \pi/12 - \rho_p d^3 l_p \pi/6$$

which transforms to

$$\rho_t D^2 T^\circ L_t = \rho_p d^3 (v^2 - 2 l_p)/2 .$$

From equation (45) it follows that

$$\rho_t D^3 k L_t = \rho_p d^3 (v^2 - 2 l_p)/2 .$$

This transforms to

$$D^3 = \frac{d^3 \rho_p (v^2 - 2 l_p)}{\rho_t L_t 2 k} \quad \text{or} \quad (47)$$

$$D = d (v^2 - 2 l_p)^{1/3} \left(\frac{\rho_p}{\rho_t L_t 2 k} \right)^{1/3} \quad \text{or} \quad (48)$$

$$\frac{D}{d} = (v^2 - 2 l_p)^{1/3} \left(\frac{\rho_p}{\rho_t L_t 2 k} \right)^{1/3} . \quad (49)$$

The ratio of crater diameter to projectile diameter D/d depends only on the material, but not on mass. For $v \gg 2 l_p$ it follows that

/30

$$\frac{D}{d} = v^{2/3} \left(\frac{\rho_p}{\rho_t L_t 2 k} \right)^{1/3} . \quad (50)$$

2.) Crater Depth and Crater Shape

According to equation (45) the depth is $T^\circ = k D$, where D is given by equation (48). The energy necessary to form this depth is given by equation (43). If the "latent" energy $E(l_p)$ in the projectile is further transformed in the crater formation process, then an additional crater volume ΔV will be formed. Since it has previously been assumed that the crater diameter is formed by the spreading of the molten projectile and that the diameter of the solidifying projectile is equal to the crater diameter, this projectile energy $E(l_p)$ is given off only in forward direction. The volume ΔV may

therefore, and because of the approximate agreement of the volumes shown in Fig. 39, be described by a cylinder with a diameter equal to the crater diameter D and of height H' , so that

$$V = D^2 \pi/4 H'. \quad (51)$$

Analogous to the above we have

$$E(L_t, \Delta V) = E(l_p) = m l_p, \quad (51a)$$

and from equations (46) and (51) it follows that

$$\rho_t D^2 H' L_t \pi/4 = \rho_p d^3 l_p \pi/6 \quad \text{or}$$

$$H'/D = 2 \rho_p d^3 l_p / (3 \rho_t L_t D^3) .$$

Substituting D^3/d^3 by the use of equation (49), we get

$$\frac{H'}{D} = \frac{4 k l_p}{3 (v^2 - 2 l_p)} . \quad (52)$$

Since the total depth is $T' = T^0 + H'$, and therefore $T'/D = T^0/D + H'/D$, it follows that

$$\frac{T'}{D} = k + \frac{4 k l_p}{3 (v^2 - 2 l_p)} = k \left(1 + \frac{4 l_p}{3 (v^2 - 2 l_p)} \right) . \quad (52a)$$

The ratio T'/D is independent of mass, and for $v \gg 2 l_p$ even independent of velocity, therefore approximately

$$T'/D = k; \quad (53)$$

this ratio depends only on the material.

On the basis of the assumptions made in equation (27) (see also Fig. 9) we have, for the ratio of measureable crater depth T to crater diameter D

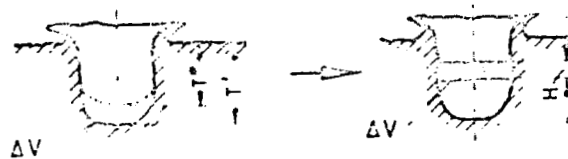


Fig. 39: Cross-Section Through a Crater for Determination of the Additional Volume ΔV .

Using the expression for diameter of equation (49), we obtain

$$\frac{T}{D} = k \left(1 + \frac{4 l_p}{3 (v^2 - 2 l_p)} - \frac{2 k \rho_t L_t}{\rho_p (v^2 - 2 l_p)} \right) \quad \text{or} \quad (54)$$

$$\frac{T}{D} = k \left(1 + \frac{2 (2 l_p - 3 k L_t \rho_t / \rho_p)}{3 (v^2 - 2 l_p)} \right) \quad (55)$$

This equation is independent of math, and for $v^2 \gg 2 l_p$ transforms into the equation

$$T/D = k = T'/D, \quad (56)$$

since h approaches zero.

3.) Crater Volume

From Equations (43), (44), and (51a), we have

$$\rho_t V(T') L_t = E_p \quad \text{or} \quad (57)$$

$$V(T') = \frac{E_p}{\rho_t L_t} = \frac{m v^2}{2 \rho_t L_t} \quad (58)$$

The measureable crater volume $V(T)$ equals the actual crater volume less the projectile volume V_p ,

(59)

From $V_p = m/\rho_p$, and from equations (58) and (59) it follows that

$$V(T) = \frac{E_p}{\rho_t L_t} - V_p = m \left(\frac{v^2}{2 \rho_t L_t} - \frac{1}{\rho_p} \right) \quad (60)$$

C. The Velocity Range E Below the Yield Point of the Projectile.

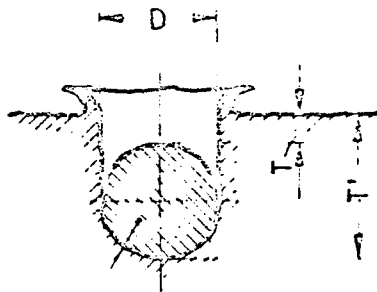
The Velocity range E is defined such that the projectile as a whole can no longer yield because its kinetic energy is too low. It is further limited by $D d$. Partial yielding of the projectile along its impacting front is not excluded. But for the purpose of estimating crater size let it now be stipulated that the entire projectile energy E_p swerves to form the crater volume $V(T')$,

$$E(L_t) = E_p \quad (61)$$

Rough statements regarding the crater depth can be made on the basis of the assumption that the projectile does not deform and, as the element that forms the crater, determines the diameter of the crater so that

$$D = d \quad (62)$$

(It would be more exact to stipulate $D \geq d$ in this range, because it was not considered that the energy transport velocity may be greater than the impact velocity.)



Projectile

From equation (62) and from geometry (see Fig. 40) we have

$$\begin{aligned} V(T') &= (T + D/2) D^2 \pi/4 + D^3 \pi/12 \text{ or} \\ V(T') &= (3 T D^2 + D^3 5/2) \pi/12. \end{aligned} \quad (63)$$

Using this equation and the relationship expressed in (46) we obtain from (61)

Fig. 40. Cross-Section of a Crater with Intact Projectiles. T = Measurable Depth, T' = Actual Depth, D = Crater Diameter = Projectile Diameter d .

$$(3 T D + D^3 \frac{5}{2}) \rho_t L_t \frac{\pi}{12} = \rho_p d^3 v^2 \frac{\pi}{12}$$

Using equation (62) it follows that

$$3 T d^2 = \frac{d^3 v^2 \rho_p}{L_t \rho_t} - \frac{5 d^3}{2} \quad \text{or} \quad (64)$$

$$\frac{T}{D} = \frac{T}{d} = \frac{v^2 \rho_p}{3 \rho_t L_t} - \frac{5}{6} .$$

From $T' = T + d$ or $T'/d = T/d + 1$ it follows (see Fig. 40) that

$$\frac{T'}{D} = \frac{T'}{d} = \frac{v^2 \rho_p}{3 \rho_t L_t} + \frac{1}{6} . \quad (65)$$

Equations (64) and (65) express the depth-diameter relationship of the craters. They are independent of mass.

As follows from equation (61), the actual crater volume $V (T')$ is given by

$$V (T') = \frac{E_p}{\rho_t L_t} = \frac{\pi d^3 v^2 \rho_p}{12 \rho_t L_t} . \quad (66)$$

VI. Evaluation of Test Results on the Basis of the Mathematical Model /33

A. Evaluation of Test Results for Equal Target Materials.

The following table II summarizes the most important equations for the two models D and E. The constants given in table II have been substituted in these equations. This results in the curves shown in Figs. 36, 41, and 42. The volume $V(T')$, shown in Fig. 36 for Pb, Al and Cu as a function of projectile velocity, agrees fairly well with the absolute values computed from equations (58) and (66).

Fig. 41 shows, for aluminum, the depth-diameter ratio T'/D and the ratio of crater diameter to projectile diameter D/d , expressed as a function of projectile velocity for the two model ranges D and E. It is evident that the test values are approximately described by the curves (absolute values).

Fig. 42 shows the calculated curves T'/D and D/d as a function of v for Pb, Cd, Ag and Cu. The ratio T'/D for different materials agrees the better with the test results shown in Figs. 31 - 33, the higher their value $\rho_t L_t$. /36
Comparison of the test data in Figs. 15 through 19 and the theoretical curves for D/d in Fig. 42 shows good agreement except for Cd, for which the values

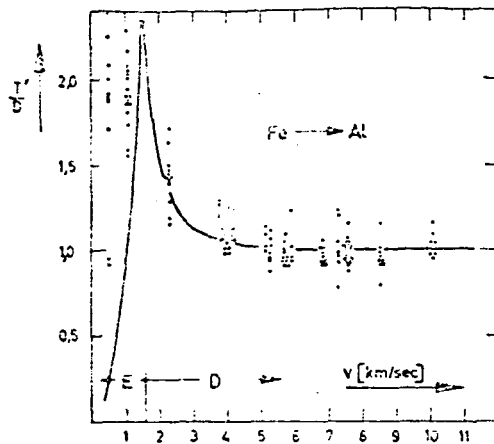


Fig. 41a

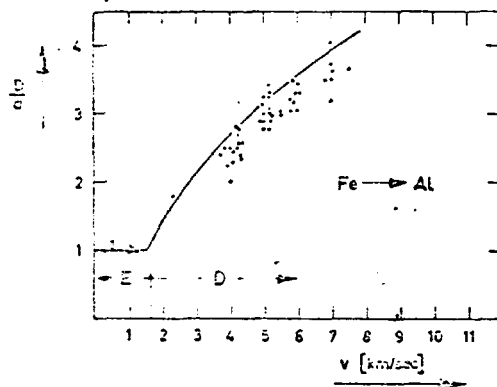


Fig. 41b

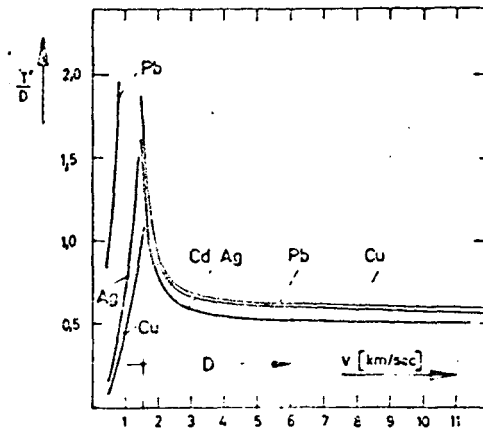


Fig. 42a

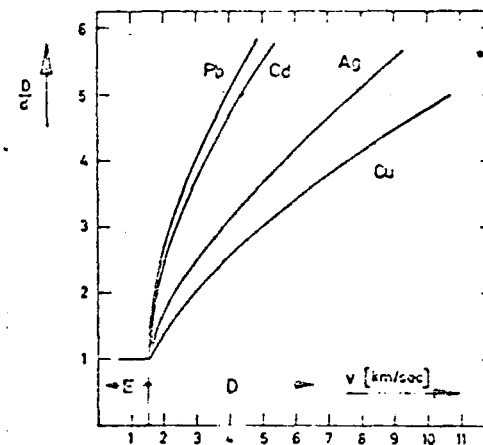


Fig. 42b

Fig. 41: Comparison of Individual Test Points with the Curves of Models D and E for Aluminum.

Fig. 41a: Ratio of Actual Crater Depth T' to Crater Diameter D , as a Function of Projectile Velocity v .

Fig. 42b: Ratio of Crater Diameter D to Projectile Diameter d as a Function of v .

Fig. 42: The Curves for Pb, Ag, Cu and Cd Corresponding to Models D and E. Fig. 42a: Ratio of Actual Crater Depth T' to Crater Diameter D , as a Function of Projectile Velocity v .

Fig. 42b: Ratio of Crater Diameter D to Projectile Diameter d as a Function of v .

are somewhat too small. As was to be expected on account of the approximation made in the model calculations, somewhat larger deviations occur along the boundary between the two model ranges. But even there the two models indicate roughly the shape of the test curves. The proportionality (D proportional to d) for the same material and for $v = \text{constant}$, as shown by the tests in Figs. 10 - 14, is satisfied by equation (49) and (42).

TABLE II: THE MOST IMPORTANT EQUATIONS FOR BOTH MODEL RANGES

Crater sizes	Model range D	Model Range E
Crater diameter	(48) $D = (v^2 - 2 L_p)^{1/3} d \left(\frac{\rho_p}{\rho_t L_t} \frac{1}{2 k} \right)^{1/3}$	(62) $D = d$
Crater diameter/ projectile diameter	(49) $D/d = (v^2 - 2 L_p)^{1/3} \left(\frac{\rho_p}{\rho_t L_t} \frac{1}{2 k} \right)^{1/3}$	$D/d = 1$
Measurable Crater depth/crater diameter	(55) $T/D = k \left(1 + \frac{L_p}{v^2 - 2 L_p} \right)^{1/3} \left(\frac{\rho_p}{\rho_t L_t} \frac{1}{2 k} \right)^{1/3}$	(64) $T/D = \frac{v^2 \rho_p}{3 \rho_t L_t} - \frac{5}{6}$
True crater depth/ crater diameter	(52a) $T'/D = k \left(1 + \frac{4 L_p}{(v^2 - 2 L_p)^3} \right)^{1/3}$	(65) $T'/D = \frac{v^2 \rho_p}{3 \rho_t L_t} - \frac{1}{6}$
True crater volume	(58) $V(T') = E_p / (\rho_t L_t)$	(66) $V(T') = E_p / (\rho_t L_t)$
Measurable crater volume	(60) $V(T) = E_p / (\rho_t L_t) - V_p$	() $V(T) = E_p / (\rho_t L_t) - V_p$
True crater volume/ projectile volume	(67) $V(T')/V_p = \frac{\rho_p v^2}{2 \rho_t L_t}$	(68) $V(T')/V_p = \frac{\rho_p v^2}{2 \rho_t L_t}$

TABLE III: CONSTANTS

Material	Velocity of sound (km/sec)	Density (g/cm ³)	Melting point L' (10 ⁸ erg)	Specific heat, c (cal/d)	Temperature increase T (°C)	Energy in Temperature increase 1, (10 ¹⁰ erg)	Crater form factor, k
Pb	1,2	11,4	2,27	0,0327	307,4	0,042	0,6
Au	1,7 - 2,1	19,7	6,45	0,0344	1043	0,150	0,43
Cd	2,3	8,65	5,4	0,0581	300,9	0,0729	0,5
Ag	2,6	10,5	10,55	0,0625	940,5	0,245	0,5
Cu	3,5	8,9	20,5	0,1045	1063	0,465	0,58
Al	5,1	2,7	40,35	0,251	640	0,671	1,00
Ti	5,1 - 6,1	4,5	40,25	0,168	1707	1,195	0,49
Ni	4,9 - 6,0	8,9	30,0	0,1332	1435	0,800	0,65
Be	12,9	1,87	108	0,665	1260	3,50	1,35
Fe		7,86	28,95	0,1355	1510	0,855	

Equations (55) and (64) satisfy the relationship T proportional to D which was found by the tests (Figs. 21 - 24) for $v = \text{constant}$. All constants, c_1 through c_6 , of the test curves can therefore be calculated from the equations given in Table II.

B. Dependence on Material.

At higher projectile velocity (roughly in excess of 3 km/sec) the craters in most materials have the shape of a semi-ellipsoid with varying eccentricity. An exception are Al and Be. These have cylindrical craters, which in the case of Al are slightly conical (this fact was taken into account in the above equations).

The functional relationship between crater volume, projectile velocity, and target material is given by equations (67) and (68). Fig. 43 shows the comparison of the calculated curve (absolute values) and the measured values, that is in the form $V(T')/V_p = f(\rho_t L_t)$. Only for Cd there is a deviation which is in excess of the range of accuracy. This may be due to the low boiling point of 767°C and the possibly related energy loss by evaporation.

Fig. 44 shows the ratio D/d as a function of the target material in the form $\rho_p / (\rho_t L_t 2k)^{1/3}$ as given by equation (49). Here too there is good agreement between the test and the theoretical curve, except for Cd. Velocity and diameter for this test were $v = 5.2$ km/sec and $d = 0.91\gamma$. The targets were Pb, Cd, Al, Ag, Au, Cu, Ti, Be and Ni. Fig. 45 shows the Stereoscan pictures for this test. Enlargement was 10,000 times for all pictures. The appreciable difference in crater size for different materials under equal impact conditions is visible in the picture.

By way of summary it can be stated that within the velocity range of 0.5 to 10 km/sec all crater sizes observed can be approximately expressed as a function of the projectile parameters by means of the equations developed from the two model ranges D and E as listed in Table II.

VII. Comparison of Craters of μ -Projectiles and cm-Projectiles.

/39

The purpose of comparing craters formed by projectiles of widely differing mass is the discovery of laws of similarity. If such laws exist it will be possible to extrapolate for even larger craters, and possibly even to formulate statements for the range of the moon craters.

Rigorously similar test conditions are a prerequisite for satisfactory comparison. Above all such tests must be performed not only with equal projectile materials but also with equal target materials. The projectile shapes must be rigorously similar, and the absolute calibration of the test units must be especially stressed.

It is not possible to evaluate directly how far these conditions are satisfied for the tests of cm-projectiles by Kineke [25] which are described in the following, as compared with the tests of μ -projectiles by the author.

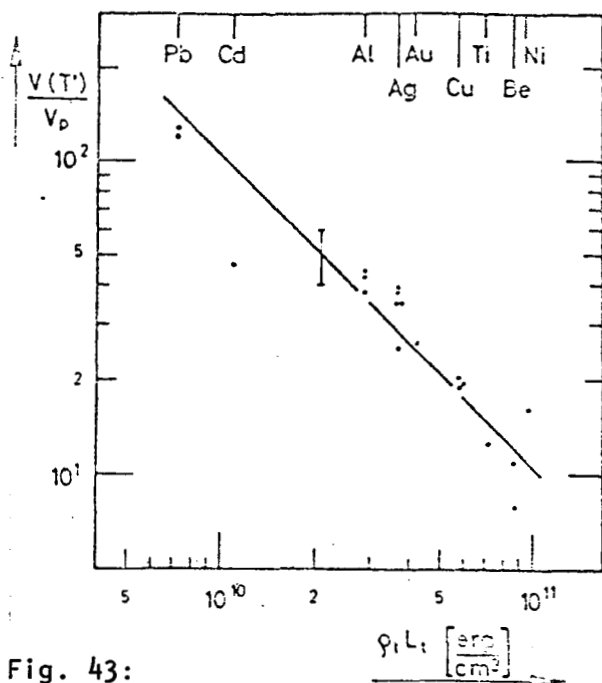


Fig. 43:

Ratio of Crater Volume to Projectile Volume $V(T')/V_p$, Expressed as a Function of $\rho_t L_t$ (Density \times Melting Energy) for Different Materials. Projectile Velocity $v = 5.2 \text{ km/sec} \pm 0.15$; Projectile Diameter $d = 0.91 \text{ } \mu \pm 10\%$.

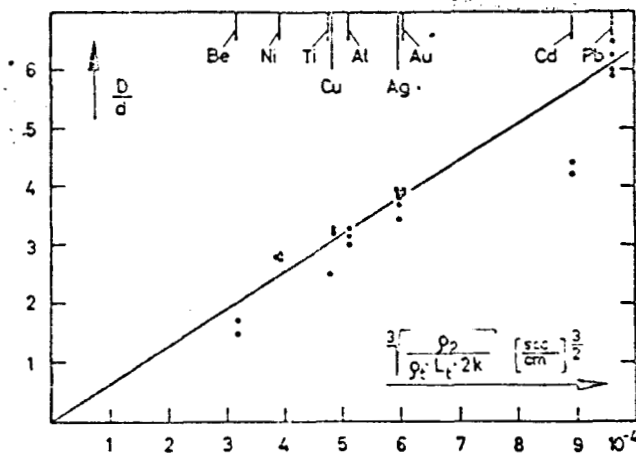


Fig. 44: Ratio D/d (Crater Diameter/Projectile Diameter) of the Measured Values, Expressed as a Function of $\rho_t L_t$ ($\rho_t L_t = 2k$) $^{1/3}$; ρ = Density, L = Melting Energy per gram, k = Crater Shape Factor.

Different target materials were used, pure materials in the tests by the author, and technical grade materials in the experiments by Kineke. Kineke further used steel projectiles of 0.18 and 8.86 grams at velocities of 1.99 to 5.47 km/sec. The shape of these projectiles is not known.

Figs. 46 - 48 show the comparison of the crater sizes in Al for both types of projectiles. Fig. 46 shows the ratio $D/m^{1/3}$ (D = crater diameter, m = projectile mass) as a function of the projectile velocity v ; Fig. 47 shows the depth-diameter ratio of the craters, T'/D , as a function of v ; and Fig. 48 shows the ratio crater volume/projectile energy, $V(T')/E_p$, as a function of v .

On the basis of the tests, Kineke derived the following equations:

$$\frac{D}{m^{1/3}} = k_1 v^{2/3}, \quad (69)$$

$$\frac{T}{m^{1/3}} = k_2 v^{2/3}, \quad \text{and} \quad (70)$$

$$V(T') = k_3 E_p, \quad (71)$$

$$d = 0.91 \mu$$

Magnification: 10 000 x

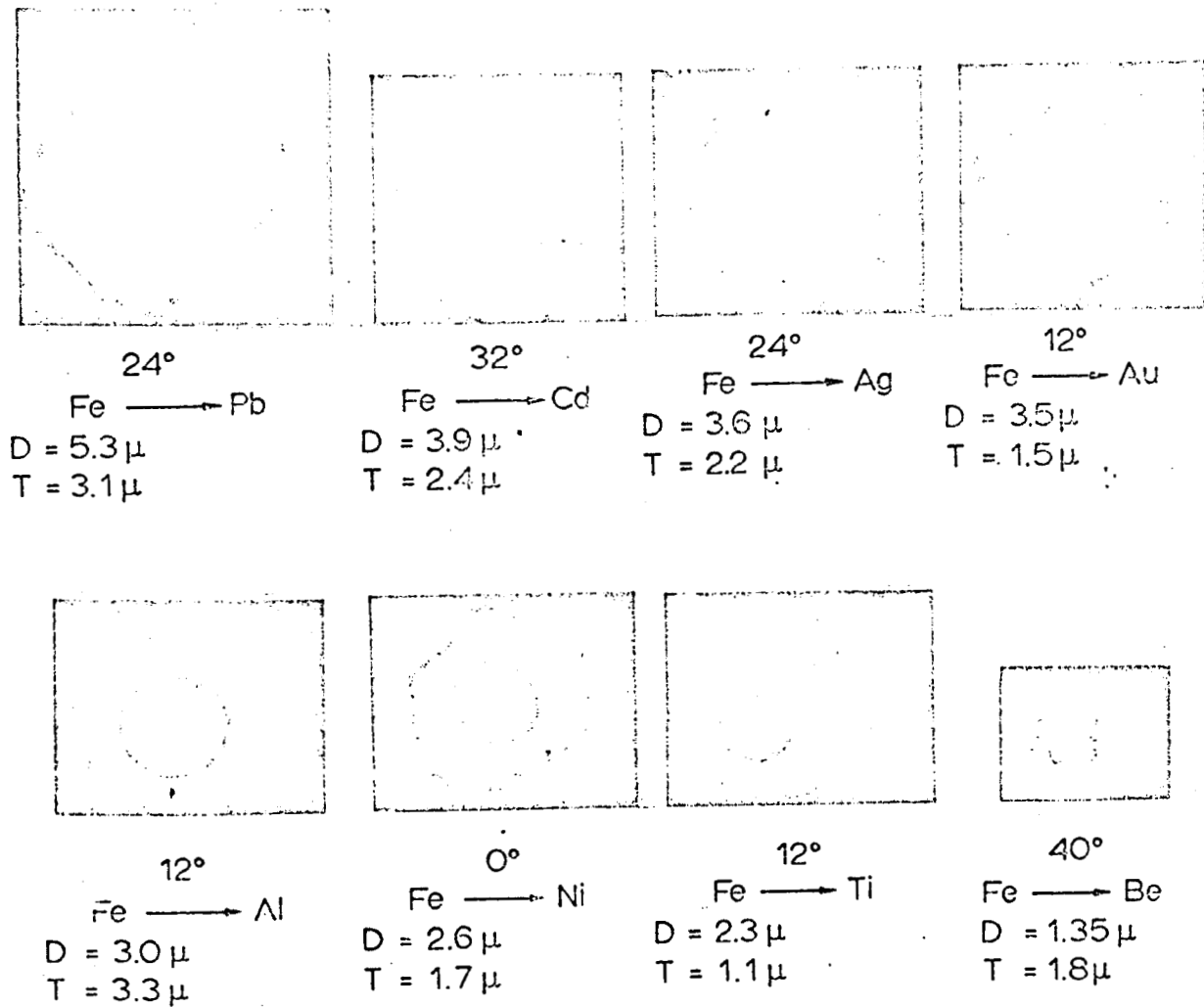


Fig. 45: Pictures of Craters Enlarged 10,000 Times, With Constant Impact. Conditions: Projectile Velocity $v = 5.2$ km/sec, Projectile Diameter $d = 0.91 \mu$.

where the constants k_1 , k_2 , and k_3 are different for particular target materials. The behavior of the functions defined by these equations corresponds for higher velocities to that of equations (49), (52a), and (58) for the μ -craters (see Table II). Table IV shows the comparison of the properties in the equations for the two projectile types and for the model D in the form:

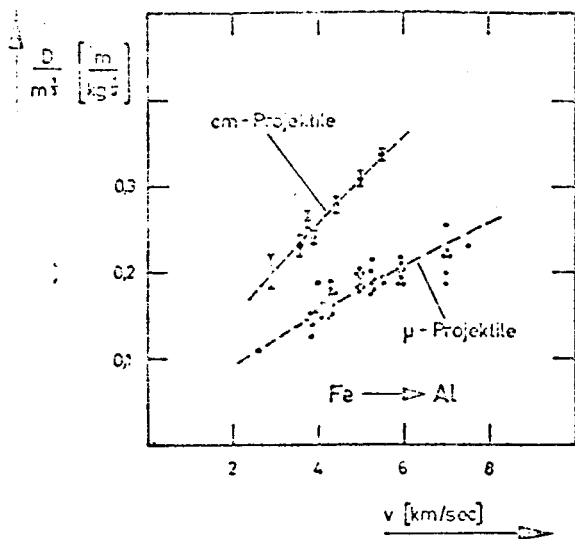


Fig. 46

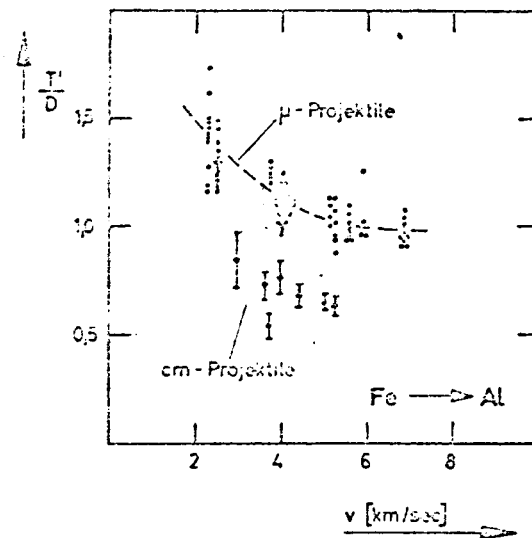


Fig. 47

Figs. 46 and 47: Comparison of the Craters Formed by μ - and cm-Projectiles, Expressed as Function of the Velocity v

Fig. 46: Crater Diameter $/m^{1/3} = f(v)$

Fig. 47: Crater Depth/Crater Diameter $T'/D = f(v)$.

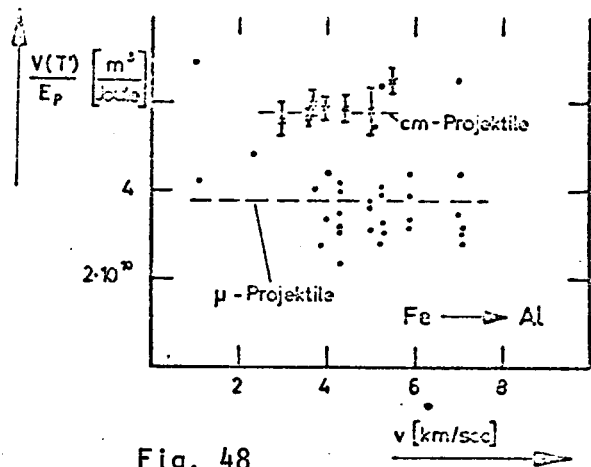


Fig. 48

Fig. 48: Comparison of the Ratio $V(T')/E_p$ Expressed as a Function of v for both Projectile Types, ρ - and cm-Projectiles, $V(T')$ = Actual Crater Volume, v = Projectile Velocity, E_p = Projectile Energy.

$$V(T')/E_p = c_8, \quad (72)$$

$$\frac{D}{m^{1/3}} = c_9 v^{2/3} \quad \text{and} \quad (73)$$

$$T'/D = c_{10}. \quad (74)$$

TABLE IV: COMPARISON OF CONSTANTS $c_8 - c_{10}$ FOR μ - AND cm-PROJECTILES

Target material	Constant	D Model	Measurements	
			μ -Projectiles	cm Projectiles
Pb	c_8	$1,352 \cdot 10^{-10}$	$1,3 \cdot 10^{-10}$	$3,02 \cdot 10^{-10}$
	c_9	$5,9 \cdot 10^{-4}$	$5,9 \cdot 10^{-4}$	$8,35 \cdot 10^{-4}$
	c_{10}		0,62	0,5
Cd	c_8	$0,913 \cdot 10^{-10}$	$0,43 \cdot 10^{-10}$	$1,00 \cdot 10^{-10}$
	c_9	$5,5 \cdot 10^{-4}$	$4,1 \cdot 10^{-4}$	$5,75 \cdot 10^{-4}$
	c_{10}		0,52	0,52
Cu	c_8	$0,168 \cdot 10^{-10}$	$0,17 \cdot 10^{-10}$	$0,5 \cdot 10^{-10}$
	c_9	$3,0 \cdot 10^{-4}$	$3,0 \cdot 10^{-4}$	$4,59 \cdot 10^{-4}$
	c_{10}		0,6	0,5
Al	c_8	$0,345 \cdot 10^{-10}$	$0,34 \cdot 10^{-10}$	$0,58 \cdot 10^{-10}$
	c_9	$3,2 \cdot 10^{-4}$	$3,6 \cdot 10^{-4}$	$(4,7 \cdot 10^{-4})$
	c_{10}		1,0	0,65

The constants c_8 and c_9 (in CGS units) are usually somewhat larger than the corresponding constants for the μ -projectile (at most by a factor of 2.5). The shape factor c_{10} , i.e. the depth-diameter ratio T'/D , in the case of Cd is equal, in the case of Pb, Cu and Al somewhat larger values are obtained for the μ -projectiles. It is not possible to check here to what degree this result may /41 be due to errors in calibration and differences in material. However, the expressions (72), (73), and (74) may be considered to be the desired similarity equations in first approximation, if one considers that the masses in these experiments differed by a factor of roughly 10^{12} , and that the respective equations are in agreement.

But exact verification of these equations or of possible deviations therefrom is possible only under rigorously similar test conditions. The solution to this problem should be worked out in cooperation of two research teams.

After construction of the dust accelerator and appurtenances, a particle filter was developed and built. Depending on electronic pre-selection, this filter permits selection of particular projectiles from the statistical particle flow according to (their) acceleration so that crater tests can be performed with particles of known mass and known velocity.

The particles used in the experiments had diameters ranging from a few tenths to several μ , and velocities of 0.5 to 10 km/sec. These projectiles were shot at targets of different materials, and the craters produced were evaluated by the use of a direct light electron microscope. In the target materials Pb, Cd, Ag, Cu, and Al, the craters were systematically measured.

A model was developed to evaluate the test curves of the crater parameters as a function of the projectile parameters. By comparison of the craters produced by cm-projectiles and craters formed μ -projectiles, similarity equations may be derived. These need to be verified in greater detail, since the impact conditions were not rigorously similar.

The author is especially indebted to Prof. W. Gentner for his guiding interest that made it possible to perform the subject investigation with modern equipment.

The author is indebted to the head of the Section for Cosmic Chemistry, Prof. J. Zaehring, who contributed substantially to the success of the investigation by his careful guidance and many helpful suggestions.

/43

The author is further indebted to Prof. K. Sitte for handling organizational problems by directing the dust accelerator section, and for aiding in the work with his advice and many discussions.

The author is further indebted to Prof. P. Rauser, Ph.D, S. Auer, Ph.D, U. Gerloff, Ph.D., and Mr. H. Ruhm, physicist, for suggestions and discussions of the paper. The author is indebted to J. Weihrauch for the microanalysis of the crater material, and for valuable assistance in the operation of the Steroscan. The author is further indebted to all members of the department who rendered assistance of technical or electronic nature.

REFERENCES

/44

1. Gerloff U., J. H. Weihrauch and H. Fechtig, *Space Res.*, Vol. VII- p. 1412, 1966.
2. Gerloff U., J. H. Weihrauch and H. Fechtig, *Naturwiss*, No. 54, p. 275, 1967.
3. Weihrauch J. H., U. Gerloff and H. Fechtig, Preprint V/7 Max-Planck-Institute for Nuclear Physics Heidelberg, to be published in *Space Res.*, Vol. VIII.
4. Gerloff U., Ph.D., thesis, University of Heidelberg, 1966.
5. Weihrauch J. H., Ph.D. thesis, University of Heidelberg, 1967.
6. Auer S., Ph.D. thesis, University of Heidelberg, 1967.

7. Baldwin R. B., *The Face of the Moon*, University of Chicago Press, 1949.
8. Baldwin R. B., *The Measure of the Moon*, University of Chicago Press, 1963.
9. Engel O. G., *6th Symp. Hypervelocity Impact*, Vol. II, No. 2, p. 337, 1963.
10. Moore H. J., Mac Cormack, D. E. Gault, *6th Symp. Hypervelocity Impact*, Vol. II, No. 2, p. 367, 1963.
11. Gault, D. E., E. D. Heitowitz and H. J. Moore, *Nasa TM X-54, 009*, 1963.
12. Hemenway C. L., J. Lincott, *Ann. of the New York Academy of Sci.*, Vol. 119, No. 1, p. 106, 1964.
13. Maurer W. C., J. S. Rinehart, *4th Symp. Hypervelocity Impact*, Vol. III, 1960.
14. Showmaker E. M., D. E. Gault, H. J. Moore, R. F. Lugn, *Am. J. of Sc.*, Vol. 261, p. 668, 1963.
15. Charters A. C., *Sc. Am.*, p. 128, 1960.
16. Atkins W. W., *4th Symp. Hypervelocity Impact*, Vol. 1, 1960.
17. Maiden C. I., J. Charest, and H. P. Ta-dif, *4th Symp. Hypervelocity Impact*, 1960.
18. Lecompte C., *Files of the German-French Research Institute, Saint-Louis*, Ref. N 29/63.
19. Partridge W. S., H. B. Van Fleet, and C. R. Whited, *J. of Appl. Phys.*, Vol. 29, No. 9, p. 1332, 1958.
20. Bjork R. L., and A. E. Olshaker, *United States Air Force Rand*, Rm-2926-Pr, 1965.
21. Schmidt R. A., K. Keil, and D. E. Gault, *National Aeronautics and Space Administration, Space Sc. Div., Ames Res. Center, Moffet Field, California*.
22. Bryan G. M., *4th Symp. Hypervelocity Impact*, 1960.
23. Bryan G. M., *5th Symp. Hypervelocity Impact*, Vol. 1, p. 511, 1961.
24. Gehring I. W., and L. G. Richards, *4th Symp. Hypervelocity Impact*, Vol. III, 1960.
25. Kineke J. H., *4th Symp. Hypervelocity Impact*, Vol. 1, 1960.
26. Maurer W. C., and J. S. Rinehardt, *4th Symp. Hypervelocity Impact*, 1960.
27. Friichtenicht J. F., *Nucl. Instr. and Meth.*, Vol. 28, No. 1, p. 70, 1964.
28. Friichtenicht J. F., and J. C. Slattery, *6th Symp. Hypervelocity Impact*, Vol. II, p. 591, 1963.
29. Rudolph V., *Zeitschr, f. Naturforsch*, Vol. 21a, No. 11, p. 1993, 1965.
- 30.
- 31.
32. Friichtenicht J. F., *Nasa CR*, p. 416, 1966.
33. Christman D. R., and J. W. Gehring, *J. Appl. Phys.*, Vol. 37, p. 1579, 1966.
34. Palmer E. P., R. W. Grow, D. K. Johnson, G. H. Turner, *4th Symp. Hypervelocity Impact*, Vol. 1, 1960.
35. Nauman R. J. *Nasa TN D-3717*.
36. Author unknown, *4th Symp. Hypervelocity Impact*, Experiment at Fort Halstead, 1961.
37. Rockowitz M., C. A. Carey, and J. F. Dignam, *5th Symp. Hypervelocity Impact*, Vol. 1, p. 535, 1961.
38. Allison, F. E., K. R. Becker, and R. Vitali, *4th Symp. Hypervelocity Impact*, Vol. 1, 1960.

39. Birkhoff G., D. P. McDougall, E. M. Pugh, and G. Tayler, *J. Appl. Phys.*, Vol. 19, p. 563, 1945.
40. Glass, C. M., *4th Symp. Hypervelocity Impact*, 1960.
41. Hill R., N. F. Mott, and D. C. Pack, *J. Appl. Phys.*, Vol. 24, p. 349, 1953.
42. Keyes R. T., R. W. Bartlett, and M. A. Cook, *4th Symp. Hypervelocity Impact*, Vol. 1, 1960.
43. Pack D. C. and W. M. Evans, *Proc. Phys. Soc.*, Vol. 64, p. 298, 1951.
44. Pugh E. M., R. J. Eichelberger, and N. Rostocker, *J. Appl. Phys.*, Vol. 23, p. 532, 1952.
45. Rostocker N., *Meteorities*, Vol. 1, 1953.
46. Kineke J. H., and R. Vitali, *6th Symp. Hypervelocity Impact*, Vol. II, No. 2, p. 457, 1963.
47. Grün E., Laboratory Term Paper, Max-Planck-Institute for Nuclear Physics Heidelberg, 1966.
48. Furth R., and M. Born, *Nature*, Vol. 145, p. 741, 1940.

Curriculum Vitae

I, Volker Rudolph, was born on September 18, 1936 at Nussloch near Heidelberg, /46 Germany, as the son of the general practitioner Willy Rudolph, M.D., and of his spouse, Margarete Rudolph, nee Pfitzer.

After attending public school in Nussloch, high school in Wiesloch, and the Lessing High School in Mannheim, from where I was graduated in March 1953, I began apprenticeship as engine fitter in the firm of Draiswerke G.m.b.H. at Mannheim-Waldhof, Germany. I completed this apprenticeship in March 1956 with journeymen's papers. Thereafter I entered high school at Wiesloch in junior class, and graduated in February 1958 (maturum).

Starting in the summer semester of 1958, I attended classes at the University of Heidelberg, Germany, with a major in physics, passing the baccalaureate examination on July 26, 1960, and graduating on May 20, 1963. Prior to starting work toward my Ph.D. thesis in November 1964, I was employed at the Max-Planck Institute of Nuclear Physics at Heidelberg, Germany. There I prepared the Diploma-thesis and my Ph.D. thesis under the guidance of Professor W. Gentner.

I am a German citizen. Since December 8, 1964 I am married to Inge Rudolph, nee Menzer.

Translated for the National Aeronautics and Space Administration under contract No. NASw-1695 by Techtran Corporation, P.O. Box 729, Glen Burnie, Maryland 21061.